Ocean Optics:
Development of Glider-Based Productivity Analysis in BC Waters Using Backscatter

by

Emily I. Koopmans

A Thesis Submitted in Partial Fulfillment of the
Requirements of the

HONOURS PROGRAM

in the School of Earth and Ocean Sciences

Supervisor: Roberta Hamme

University of Victoria

We acknowledge and respect the Lək̓ʷəŋən (Songhees and Xʷsepsəm/Esquimalt) Peoples on whose territory the university stands, and the Lək̓ʷəŋən and W̱SÁNEĆ Peoples whose historical relationships with the land continue to this day.

1. Abstract

The ocean plays a crucial role in regulating atmospheric carbon dioxide yet quantifying the processes that govern its carbon storage remains a challenge. The biological pump, which converts dissolved carbon into organic particles through biological processes, is a key component of this cycle. While some particles remain suspended in the upper ocean, others sink, either individually or as larger aggregates, contributing to long-term carbon sequestration. Understanding the distribution and size of these particles is essential, but measurements are difficult to obtain since particle dynamics fluctuate with biological activity, ocean currents, and seasonal changes. Optical backscatter offers a valuable tool to address this challenge.

We developed a method to process backscatter sensor data from autonomous ocean gliders, adapting a technique originally designed for Argo floats. Our approach partitions raw backscatter into three components: scattering from large aggregates, smaller particles, and instrument noise. A two-filter method was used to isolate scattering from small particles, while the deepest backscatter measurements provided an estimate of background noise. The remaining signal was attributed to large aggregates.

We applied this method to data from a Canadian-Pacific Robotic Ocean Observing Facility (C-PROOF) glider mission in offshore British Columbia waters. By comparing size-resolved backscatter and chlorophyll fluorescence, we observed distinct differences in particle dynamics, with small-particle backscatter strongly correlated with chlorophyll and large-particle backscatter showing weaker associations. We identified contrasting high-productivity regions: one dominated by smaller particles, and another dominated by large aggregates. These patterns

suggest that areas with similar chlorophyll concentrations can differ significantly in their potential for carbon export, depending on particle composition and sinking behavior.

This approach also revealed important oceanographic features, including a subsurface chlorophyll maximum, sediment resuspension layers, and a small but persistent zone of elevated productivity likely influenced by large-scale ocean circulation. These features highlight how regional carbon export can be enhanced by subtle physical changes such as fronts or circulation boundaries—emphasizing the need to consider both biological and physical drivers when studying oceanic carbon cycling.

By enabling size-resolved analysis of particulate matter, our method enhances the utility of gliders for carbon cycle research. Its application across other missions could help identify export hotspots, track seasonal variability, and improve estimates of oceanic carbon sequestration in a changing climate.

2. List of Figures

3. Introduction and Background

As a major regulator of the global carbon cycle, the ocean plays a crucial role in modulating atmospheric carbon dioxide (CO_2) levels and Earth's climate through interconnected physical, chemical, and biological processes. It is a significant carbon sink, absorbing approximately 25% of anthropogenic CO_2 emissions (Friedlingstein et al., 2025). Dissolved CO_2 is stored in surface waters or transported to deeper layers, helping to buffer rising greenhouse gas concentrations and moderate climate change (Boyd et al., 2019).

The biological carbon pump is a broad term encompassing various processes that regulate atmospheric CO_2 concentrations. One of these processes is the gravitational pump, which transfers carbon from the euphotic zone to the subsurface ocean via sinking organic particles (Claustre et al., 2021). These particles are produced in the surface waters where phytoplankton convert dissolved CO_2 into organic matter through photosynthesis (Giering & Humphreys, 2017). When the phytoplankton die or are consumed, their remains, along with other carbon-rich particles such as zooplankton fecal pellets, sink through the water column (Nowicki et al., 2022). The efficiency of the gravitational pump is determined by how long carbon remains stored away from the atmosphere, with deeper storage leading to longer retention times (Boyd et al., 2019). Changes in the export of particulate organic carbon (POC) could alter atmospheric CO_2 uptake, ultimately impacting the climate (Kwon et al., 2009).

A substantial fraction of sinking POC is transported in the form of aggregates, clusters of smaller particles that coagulate under specific conditions (Barkmann et al., 2010). Aggregate formation is influenced by factors such as particle concentration, stickiness, and collision rate (Karakaş et al., 2009). The sinking velocity of these aggregates is influenced largely by size but is also dependent on composition and porosity (Bach et al, 2016). While large aggregates play a critical role in exporting carbon to deeper layers, their distribution and behaviour remain poorly understood, largely due to the challenges of measuring sinking material in the ocean (Briggs et al., 2011).

Quantifying the processes of the biological carbon pump is inherently difficult due to the vast scale of the ocean and the limitations of current measurement techniques. Many existing approaches focus on assessing particle concentration, primary productivity, and export flux, yet each comes with constraints (Giering et al., 2020). Satellite remote sensing provides large-scale chlorophyll concentrations and primary productivity estimates but is restricted to surface waters (Antoine et al., 1996). Sediment traps offer direct particle flux measurements but have limited spatial and temporal coverage (Martin et al., 1987; Fischer et al., 2016). Radioisotope tracers such as Thorium-234 can estimate particle export but provide limited insight into particle size distribution (Buesseler et al., 1998). Dissolved biogeochemical tracers (e.g., nutrients, oxygen) allow for broad-scale assessments of POC flux but do not directly track the sinking and transformation processes of particulate matter (Gehlen et al., 2006). Pumping and bottle-based techniques can collect POC measurements across different depths and conditions but are prone to sample contamination and limited representation of particle size distributions (Moran et al., 1999). These traditional approaches are unable to effectively and efficiently isolate and map both large aggregates and smaller suspended particles separately, creating a key gap in understanding the ocean's carbon cycle.

This study addresses this gap by developing a generalized method for processing optical backscatter data collected by autonomous ocean gliders. Optical backscatter sensors measure light scattering by suspended particles, providing a proxy for suspended particulate matter (Downing, 2006). However, distinguishing between large fast-sinking aggregates and smaller particles remains challenging. This study presents a processing approach that can be applied to optical sensors across different glider platforms, improving the characterization of particle size distributions in diverse oceanographic settings. This method is demonstrated using a glider mission along Line P, but it is designed for application across other glider missions. By applying this approach to different datasets, we can improve the monitoring of particulate carbon transport and refine assessments of the biological carbon pump's role in oceanic carbon sequestration.

Previous studies, such as Briggs et al. (2020), have used optical backscatter sensors on Argo floats to estimate particle size distributions and carbon flux. Briggs et al. (2020) demonstrated that particle fragmentation plays a major role in regulating biological CO_2 sequestration, emphasizing the significance of particle dynamics in the water column. Their work showed that Argo floats, deployed for extended periods of up to five years, can measure particle size distributions and track carbon flux, though their profiling mode limits horizontal resolution. Argo floats are generally not designed to be recovered, and their routes are dictated by ocean currents, meaning they cannot be directly controlled (Argo, n.d.).

In contrast, autonomous gliders are reusable and remotely operated, offering continuous data collection along a transect during shorter-term deployments (Teledyne Webb Research, 2012). This study builds on Briggs et al.'s backscatter approach by adapting and refining it for use on gliders, allowing for enhanced resolution of particle size distributions and transport dynamics along Line P and beyond.

3.1 Oceanic Particle Dynamics

The efficiency of the biological carbon pump is determined by how long carbon remains stored away from the atmosphere, with deeper storage leading to longer retention times (Boyd et al., 2019). The depth of storage is influenced by the export of sinking particulate organic carbon from the surface ocean, which varies based on particle size, composition, and settling behavior (Claustre et al. 2021). Aggregates (clusters of smaller particles) are among the primary contributors to deep-sea carbon sequestration (Hayashi, 2023). Understanding the spatial and temporal distributions of these large aggregates and their constituent smaller particles is essential for assessing past carbon sequestration and predicting its future dynamics in a changing climate.

Large, fast-sinking aggregates play a key role in transporting organic matter to the deep ocean, where they influence nutrient distributions, support deep-sea ecosystems, and regulate atmospheric CO_2 levels (Weber et al., 2016). However, only organic matter that sinks beyond 1000 m is considered sequestered on centennial timescales, while the majority is respired before reaching this depth (Claustre et al., 2021). While larger aggregates generally contribute more to deep ocean carbon flux than smaller particles, flux is not solely determined by size. Other factors, such as particle composition, porosity, and environmental conditions (ocean currents, turbulence, aggregation-fragmentation dynamics, etc.) also play a critical role in controlling sinking behaviour and carbon export efficiency (Giering & Humphreys, 2017).

Although this study primarily focuses on particle concentration and size distributions, interpreting carbon flux dynamics requires considering these additional variables. Variability in aggregate formation, fragmentation, and degradation processes ultimately influences the efficiency of the biological carbon pump and the extent of long-term carbon sequestration in the deep ocean.

3.2 Optical Backscatter

Optical backscatter sensors provide a powerful tool for quantifying suspended particulate matter in marine environments, offering insights into particle distribution and dynamics throughout the water column (Briggs et al., 2020). These sensors operate by detecting light scattering as it interacts with suspended particles, enabling real-time, non-invasive monitoring of particulate matter across spatial and temporal scales (WETLabs ECO-BB9).

At the core of optical backscatter technology is the interaction between incident light and suspended particles. When a light source, typically a laser or LED, emits a beam, into the water, particles scatter the light in various directions (WET Labs. 2007). The angular distribution of this scattered light is described by the volume scattering function (VSF), which characterizes how much light is scattered at different angles relative to the incident beam (Freda, 2012). Backscatter sensors measure at a fixed angle, capturing only a single point on the VSF curve (Freda, 2012). A photodetector positioned at the fixed angle relative to the incident beam records the intensity of backscattered light (Figure 3.1). The strength of this signal is influenced by both the concentration and size distribution of particles in the water (Downing, 2006).

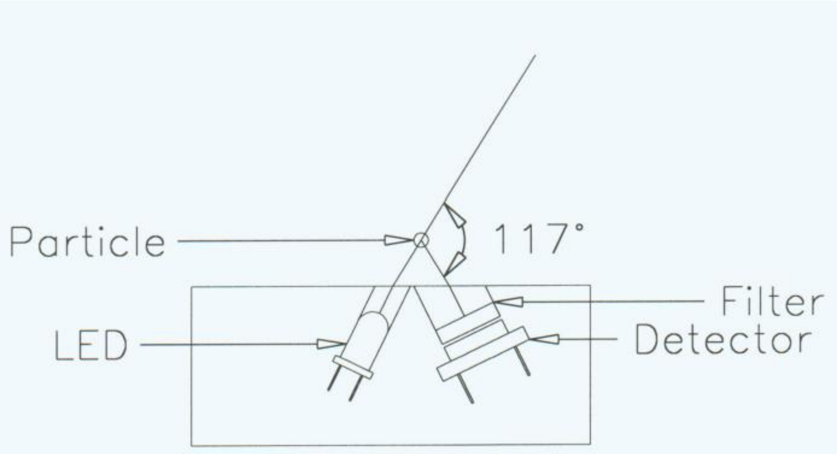

Figure 3.1 Simple Configuration of a WET Labs ECO Scattering meter at 117°. Reproduced from WET Labs. (2007). ECO BB9 user manual. https://www.comm-tec.com/prods/mfgs/Wetlabs/Manuals/Eco-BB9_manual.pdf.

The intensity and angular distribution of scattered light are governed by multiple factors, including particle size, shape, refractive index, and composition (Downing, 2006). Larger particles typically produce stronger backscatter signals, whereas smaller particles scatter light more diffusely. Properties such as particle angularity and reflectivity also influence scattering behaviour (Downing, 2006). However, for the scope of this study, we do not consider these potential effects and focus on particle concentration and size distribution as the primary determinants of backscatter signals.

A single photodetector measures bulk optical properties like backscattering, which correlate with particle concentration. While it can't resolve individual particles, larger aggregates (~>100 µm) cause brief spikes in the signal, allowing them to be distinguished from smaller background particles (Figure 3.2). This method enables estimates of particle concentration, POC flux, and size, providing valuable insights into oceanic particle distributions.

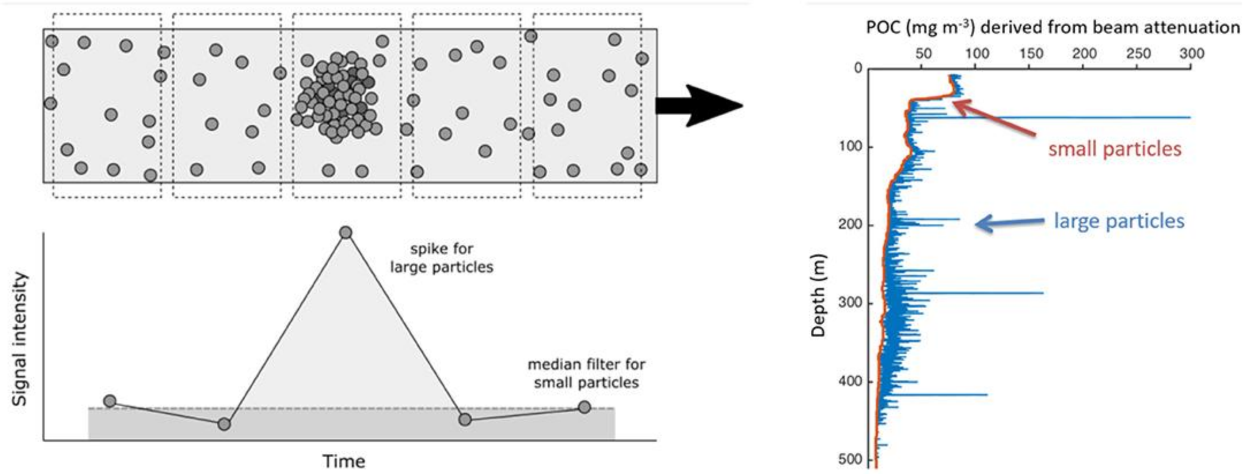

Figure 3.2 Processing method for distinguishing small and large particles from a single photodetector. A median filter is applied to estimate the background signal from small particles, while brief spikes in the signal indicate the presence of large particles. Reproduced from *Sinking Organic Particles in the Ocean—Flux Estimates From in situ Optical Devices* by Giering, S. L. et al. (2020), *Frontiers in Marine Science*, 6, 2296-7745. https://doi.org/10.3389/fmars.2019.00834.

The bulk backscattered light is quantified using the optical backscattering coefficient (b_b, m^{-1}), which represents the fraction of light scattered in the backward direction per unit distance travelled (Mantovanelli & Thomson, 2016). However, a portion of the backscatter signal originates from molecular scattering by seawater itself. To isolate the contribution of suspended particles, the particulate backscattering coefficient (b_{bp}, m^{-1}) is derived by subtracting the seawater contribution from the total backscatter signal (Zhang et al 2019).

This research focuses on partitioning b_{bp} to distinguish between scattering contributions from large particle aggregates, smaller suspended particles, and instrument-related noise, thereby improving the accuracy of particulate carbon transport assessments.

3.3 Gliders

Autonomous underwater gliders have revolutionized oceanographic research by providing cost-effective, energy-efficient, and long-duration monitoring of marine environments (Laurent, 2017). These remotely operated vehicles can operate for months at a time, collecting uncontaminated *in situ* data during both descent and ascent (Teledyne Webb Research, 2012).

Gliders adjust their buoyancy by drawing in or expelling small amounts of oil from an internal reservoir, altering their density relative to the surrounding seawater (Teledyne Webb Research, 2012). As the glider sinks or rises, its hydrodynamic wings convert vertical motion into forward thrust, propelling it through the water in a sawtooth trajectory (Figure 3.3). This propulsion method eliminates the need for traditional propellers, significantly reducing energy consumption and allowing for extended missions (C-PROOF Platforms).

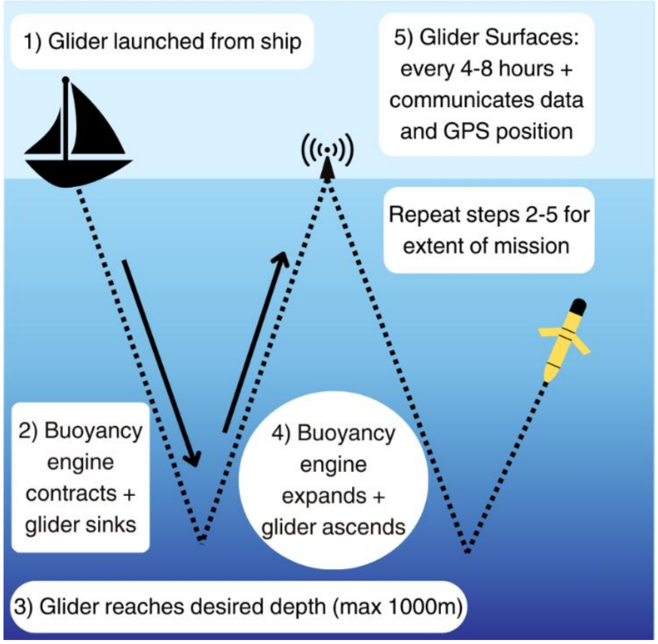

Figure 3.3 How a glider operates and moves in a sawtooth pattern. Created using information on the C-PROOF platforms page.

The glider used in this study, along with its data, was collected and provided by the Canadian-Pacific Robotic Ocean Observing Facility (C-PROOF) and more information is available at https://cproof.uvic.ca. The deployed glider is a Slocum G2 1000m model, designed to operate at depths of up to 1000 meters. These gliders are widely used to measure oceanographic parameters across diverse environments worldwide (Teledyne Webb Research, 2012). Travelling at a speed of 20–30 km per day, they periodically surface to receive satellite GPS updates and transmit collected data. The C-PROOF gliders are equipped with sensors that measure ocean temperature, salinity, dissolved oxygen, chlorophyll, CDOM and backscatter. (C-PROOF Platforms).

The use of autonomous underwater gliders in this study directly addresses the challenges outlined in the introduction by providing a novel approach to monitoring particulate organic carbon (POC) transport in the ocean.

3.4 Study Objectives and Significance

Despite advances in understanding the biological carbon pump, significant gaps remain in quantifying particulate organic carbon flux, particularly in mapping the distributions of large, faster-sinking aggregates and smaller particles (Briggs et al., 2020). Traditional methods, such as sediment traps and satellite remote sensing, provide valuable insights but are limited in spatial and temporal coverage or restricted to surface waters (Giering et al., 2020). Autonomous underwater gliders equipped with optical backscatter sensors offer a cost-effective, energy-efficient solution, enabling high-resolution, in situ measurements throughout the water column (Teledyne Webb Research, 2012). By leveraging glider-based measurements along Line P, this study improves our ability to track particulate carbon flux, addressing key gaps in understanding the biological carbon pump's efficiency and role in long-term carbon sequestration.

This study developed a generalized processing method for interpreting optical backscatter data from sensors mounted on ocean gliders, enhancing the ability to differentiate between various particle-size classes. While applied to data collected along Line P, the methodology is designed to be adaptable to different glider platforms and oceanographic regions. By adapting and creating techniques for analyzing optical backscatter signals, this research enhances our ability to track particulate carbon flux and assess the efficiency of the biological carbon pump, contributing to a broader understanding of oceanic carbon sequestration.

4. Method Development

In this study, we developed an algorithm to process the particulate backscattering coefficient (b_{bp}) for glider-based measurements. While the general framework for backscatter processing was originally designed for Argo floats (Briggs et al., 2020), it could not be directly applied to gliders due to fundamental platform differences. Additionally, we undertook an in-depth review of their methodology to clarify the reasoning behind each step and create a method to suit the unique characteristics of glider data.

The development of the method required reprocessing raw data to confirm measurement units, identifying and correcting sensor saturation, and partitioning b_{bp} into separate optical backscattering components. Although our approach was informed by the Briggs methodology, adapting it for gliders required significant modifications to account for their continuous profiling behavior, higher data resolution, and inherent platform differences. Potential sources of error, including sensor saturation, the exclusion of some profiles, and limited deep-cast data, were addressed and quantified where possible. The steps outlined below describe the procedures for data collection, processing, and analysis.

4.1 Glider Data

All glider data we analyzed in this study was collected by a Slocum G3 Deep autonomous ocean glider (ID: dfo-rosie713) nicknamed “Rosie”, deployed by C-PROOF. The glider was equipped with multiple sensors, including a Wet Labs FLBBCDSLC combined three-channel sensor to measure particulate optical backscattering b_{bp} at 700 nm. Additional sensors for other measurements are listed in Table 4.1. The glider data is available on C-PROOF’s deployment webpage (https://cproof.uvic.ca/gliderdata/deployments/dfo-rosie713/dfo-rosie713-20230810/).

The glider was deployed on 3 Aug 2023 from the *CCGS John P. Tully* research vessel, following Line P from offshore Tofino, British Columbia, to Ocean Station Papa (50°N, 145°W) in the northeast Pacific (Figure 4.1). It completed its mission and returned to Tofino for recovery on 16 Nov 2023, collecting data during the outbound and return. The data was compiled into profiles of either downcasts or upcasts along its trajectory. The glider descended to depths of 1000m for each profile except in the shallower region by the coast. However, the optics were turned off after 200m for most of the profiles to conserve battery power.

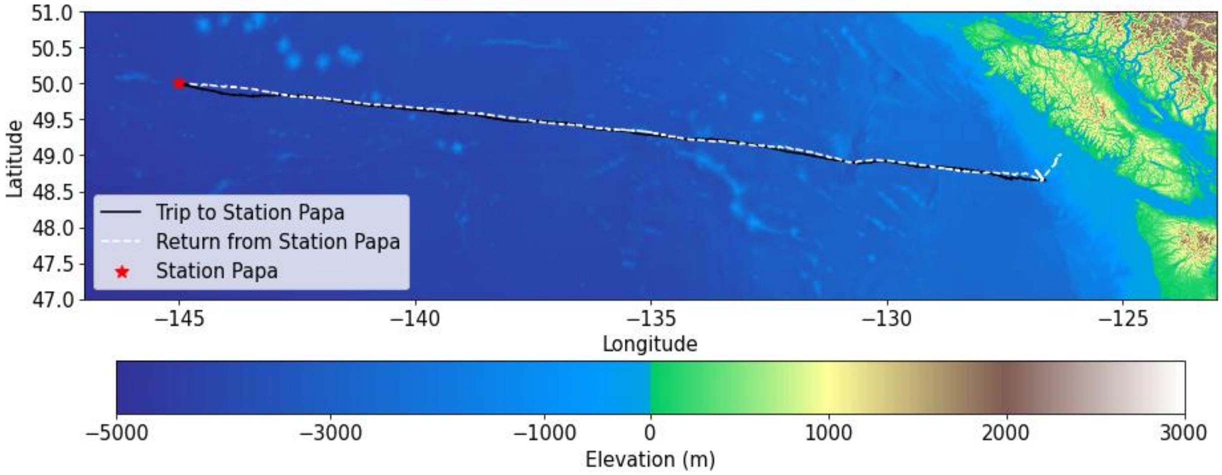

Figure 4.1 Bathymetric and Topographic map of the C-PROOF glider's trajectory. The black line is the outbound trip from offshore Tofino to Ocean Station Papa (red star), following Line P. The white dashed line is the return trip to Tofino.

Table 4.1 Glider Sensor Details

Oceanographic Measurement	Make	Model
CTD	Seabird	SlocumCTD
Optics	WetLabs	FLBBCDSLC
Oxygen	AADI	Optode4831
Pressure*	Micron	Pressure

*The Micron pressure sensor is used to regulate the glider's buoyancy, whereas the CTD records pressure measurements.

4.2 Processing Particulate Backscattering Data (b_{bp})

4.2.1 Conversion of Raw Counts to Volume Scattering Function

As discussed earlier, optical backscatter sensors detect scattered light intensity, which the glider reports in two forms: counts and the volume scattering function, abbreviated as VSF or β(θ), in units of m^{-1} sr^{-1}. The counts are the direct measurement of light intensity, and the sensor has been calibrated according to Wet Labs calibration equation (equation (1)) to convert them to the VSF. Initially, it was unclear if the provided "backscattering" data was still the VSF or if it had undergone further processing to the particulate backscatter coefficient (m^{-1}). To confirm that this data was the VSF, the raw counts were reprocessed using calibration equation (1):

$$(1)\quad \beta(\theta) = \text{Scale Factor} \times (\text{Output} - \text{Dark Counts})$$

For the 700 nm sensor, the scale factor (2.090×10^{-6} m^{-1} sr^{-1}/ counts) and dark counts (44 counts) were obtained from the manufacturer's testing certification. The output values were taken directly from the glider's raw count measurements. Reprocessing confirmed the provided dataset was the VSF (m^{-1} sr^{-1}) and had not been converted to the particulate backscattering coefficient (m^{-1}).

4.2.2 Sensor Saturation and Data Filtering

Upon inspection, we observed that the data exhibited a saturation point at approximately 0.008539 sr^{-1} m^{-1}, beyond which signals were not accurately detected and instead were recorded as the maximum value. This resulted in large regions of flattened data (Figure 4.2).

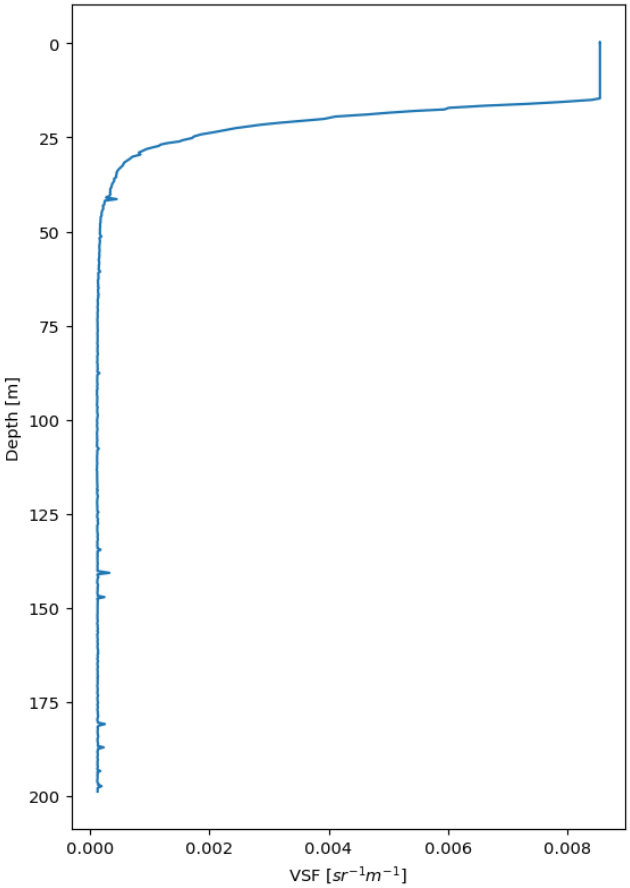

Figure 4.2 An example depth (m) profile displaying the volume scattering function (VSF sr^{-1} m^{-1}) when the optical sensor was saturated. The profile was collected on 26 Sept 2023, from 3:52 to 5:26 UTC. The profile began at 49° 49' 34.09" N and 143° 7' 1.33" W.

To further investigate this issue, we analyzed additional glider deployments to compare saturation points. Alongside the dfo-rosie713-20230810 deployment, we examined an earlier Rosie mission (dfo-rosie713-20220531) to determine whether it exhibited similar sensor saturation. Additionally, two deployments of the “Walle” glider (dfo-walle652-20191209 and dfo-walle652-20210121) were analyzed for comparison. All three of these missions were Line P deployments obtained through the C-PROOF Deployments page (https://cproof.uvic.ca/deployments/index.html).

This analysis, along with consultation with the C-PROOF team, confirmed that the saturation point was sensor-specific and dependent on the gain setting. For example, the dfo-walle652 glider, which also collected data along Line P, had a lower saturation threshold of 0.0065952 sr^{-1} m^{-1}. Since these optical backscatter sensors operate within a ±5 V range, excessive backscatter intensity leads to saturation. While adjusting the gain can mitigate this issue, it presents a trade-off: a higher gain increases the risk of saturation, while a lower gain reduces sensitivity to weak signals, potentially obscuring finer details within the instrumental noise.

Interestingly, we found that all saturated profiles occurred during downcasts. The reason for this pattern is unclear, and further investigation would be necessary to determine whether it is due to physical, environmental, or sensor-related factors. As this was beyond the scope of our study, we opted to remove these profiles from the dataset.

A total of 43 saturated profiles were removed. We excluded entire profiles rather than individual data points, as the sensor appeared to take time to readjust following saturation (see the sharp decline in Figure 4.2 from ~20-30 m). The removed profiles were relatively well distributed throughout the deployment, rather than concentrated in a single location, except for one cluster that aligned with a highly productive region discussed later in the discussion section (Figure 4.3). This decision was consistent with the methodology of Briggs et al. (2020), where large values, likely representing live zooplankton, were excluded to prevent artifacts in the dataset. While this approach minimized errors from saturation, it potentially removed significant large or small spikes

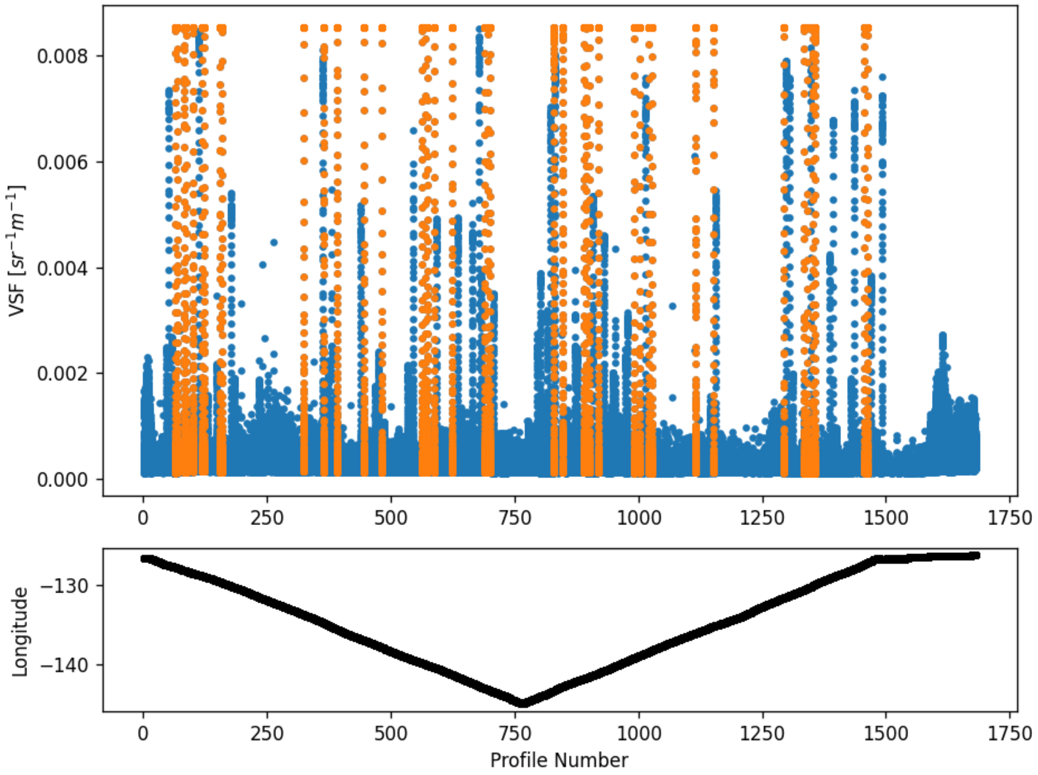

Figure 4.3 VSF (sr^{-1} m^{-1}) for glider profiles along Line P. The blue dots in Plot A, are the original dataset, and the orange dots are the profiles that were removed from sensor saturation. Plot B shows the longitude along Line P of the profile number.

4.2.3 Conversion of VSF to Particulate Backscattering Coefficient

The volume scattering function (VSF) in sr^{-1} m^{-1} was converted to the particulate backscattering coefficient (b_{bp}) in m^{-1} (Figure 4.4) using Equation (2) (Briggs et al., 2020):

(2) $b_{bp}\,(m^{-1}) = 2\pi\chi \cdot (VSF - \beta_{sw})$

where $\chi = 1.076$ (SeaBird Scientific, 2024), and β_{sw} is the scattering due to seawater. The β_{sw} values were calculated using a MATLAB function developed by Zhang et al. (2019). This function utilized sensor-specific parameters, including wavelength (700nm) and scattering angle (~124^{o}), as well as environmental inputs: temperature (^{o}C), absolute salinity (salinity in PSU*1.0047), pressure (dbar), and the depolarization ratio. The model default of 0.039 was used for the depolarization ratio, assuming it to be constant despite variations in pressure (Zhang et al 2019).

The MATLAB function provided two outputs: the spectral volume scattering and the total scattering coefficient. The spectral volume scattering was used as it has the same units as VSF (Zhang et al 2019). At the beginning of the deployment, a few profiles lacked salinity measurements making it impossible to accurately calculate β_{sw}. These profiles were left out of the final dataset.

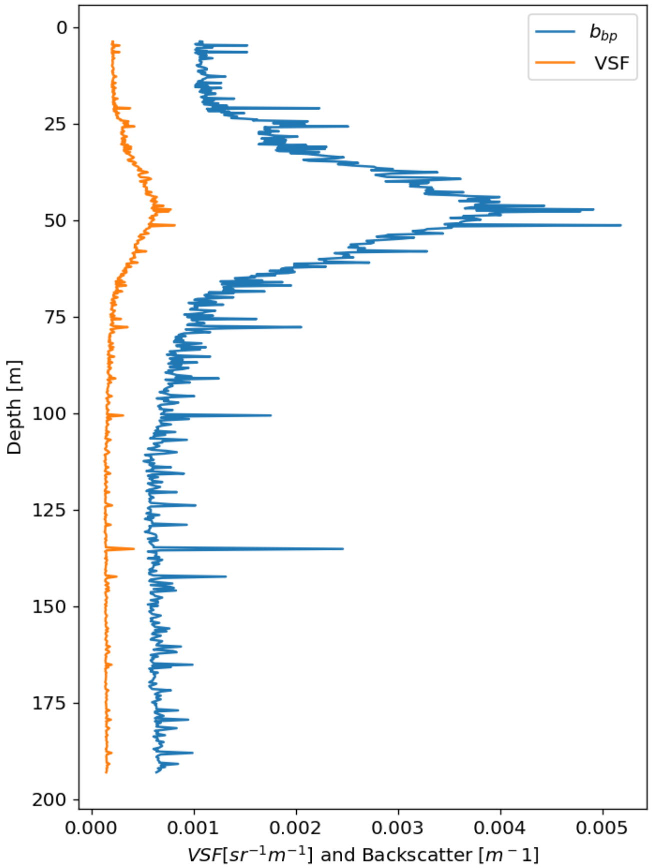

Figure 4.4 An example depth (m) profile comparing the VSF (sr^{-1} m^{-1}) to the particulate backscattering coefficient (*bbp* m^{-1}). The profile was collected on 20 Aug 2023 from 12:32 to 14:03 UTC. The profile began at 48° 52' 48.10" N and 129° 39' 8.52" W.

4.3 Partitioning b_{bp} into Components

The particulate backscattering coefficient (b_{bp}) was separated into three components as described by Briggs et al. (2020):

$$b_{bp} = b_{bl} + b_{bs} + b_{br}$$

b_{bl}: Backscattering from large particles

b_{bs}: Backscattering from small, labile particles

b_{br}: Instrument blank including refractory particles.

4.3.1 Isolating Optical Backscattering from Small Particles (b_{bs})

To effectively isolate b_{bs} while preserving key data structures, we applied a sequential running minimum and maximum filter to the glider dataset, with adjustments made to account for the increased data density of a glider compared to Argo float observations (Briggs et al., 2020). Applying a running minimum, followed by a running maximum filter to the optical data is ideal for preserving key structures and trends in the dataset while removing local "spikes" or fluctuations. The minimum filter captures the lower boundary, reducing random positive spikes (e.g., larger aggregate particles in the water column). The maximum filter restores the large-scale features that may have been suppressed by the minimum filter. An alternative is a running median filter, but this method blends out both high and low spikes which could unintentionally overestimate b_{bs} and lose some of the smaller trends.

We chose a running filter that introduced a mirroring effect at the beginning and end of each profile due to the absence of data points required for the initial windows. To create the first window, the filter extends the dataset by mirroring the first points at the start, generating "ghost points" that allow the window to function correctly. Figure 4.5 illustrates this process using a five-point running minimum filter on a hypothetical dataset. In Figure 4.5a, the first filter window is centred on the first actual data point but incorporates two mirrored points to compensate for missing values. The minimum of this window is then recorded. In the second window (Figure 4.5b), only one ghost point is used, and by the third window (Figure 4.5c), the filter operates solely on actual data points. This effect has a relatively low impact on our analysis since these ghost points are either at the surface of the mixed layer, which should be homogeneous or at the bottom, which should have low particle concentration.

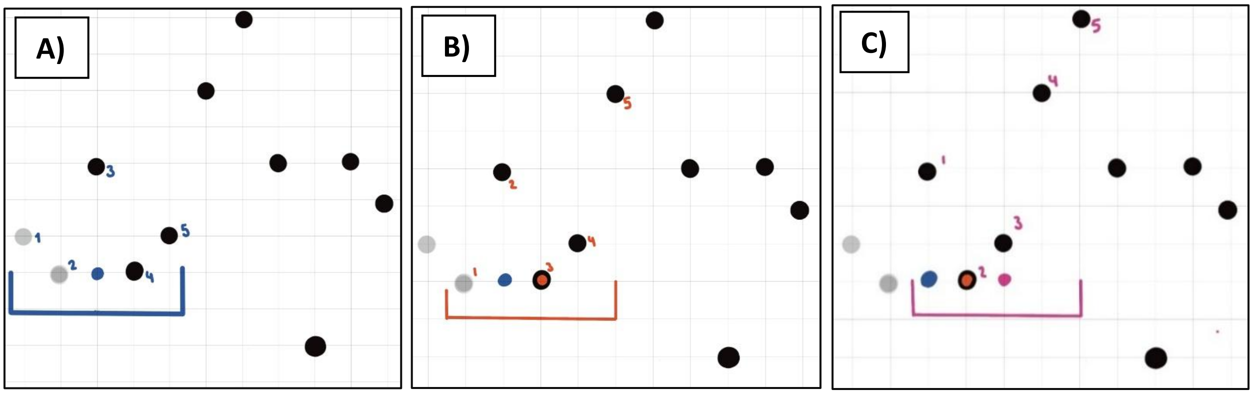

Figure 4.5 A hypothetical dataset displaying the application of a five-point running filter. A) The first window is displayed in blue. The grey points are mirrored data points, and the blue dot is the minimum in the window. B) The second window is displayed in red; the red dot is the minimum in the window and the blue dot is the minimum from the previous window. C) The third window is displayed in pink; the pink dot is the minimum in the window and the red and blue dots are the minimums of the previous two windows.

When applied to a larger version of the hypothetical dataset, as shown in Figure 4.5b, the five-point minimum filter effectively removed large spikes; however, it also attenuates some broader data trends. To counteract this smoothing and recover lost variability, a corresponding maximum filter is subsequentially applied to the results of the minimum filter (Figure 4.6c).

The same technique was applied to each profile from the glider's optical dataset (Figure 4.7) except a 43-point running window was used. Briggs et al. (2020) originally utilized an 11-point window filter optimized for Argo float data; however, because gliders collect data at a higher resolution per meter, a larger window was necessary. If the dataset size increases while

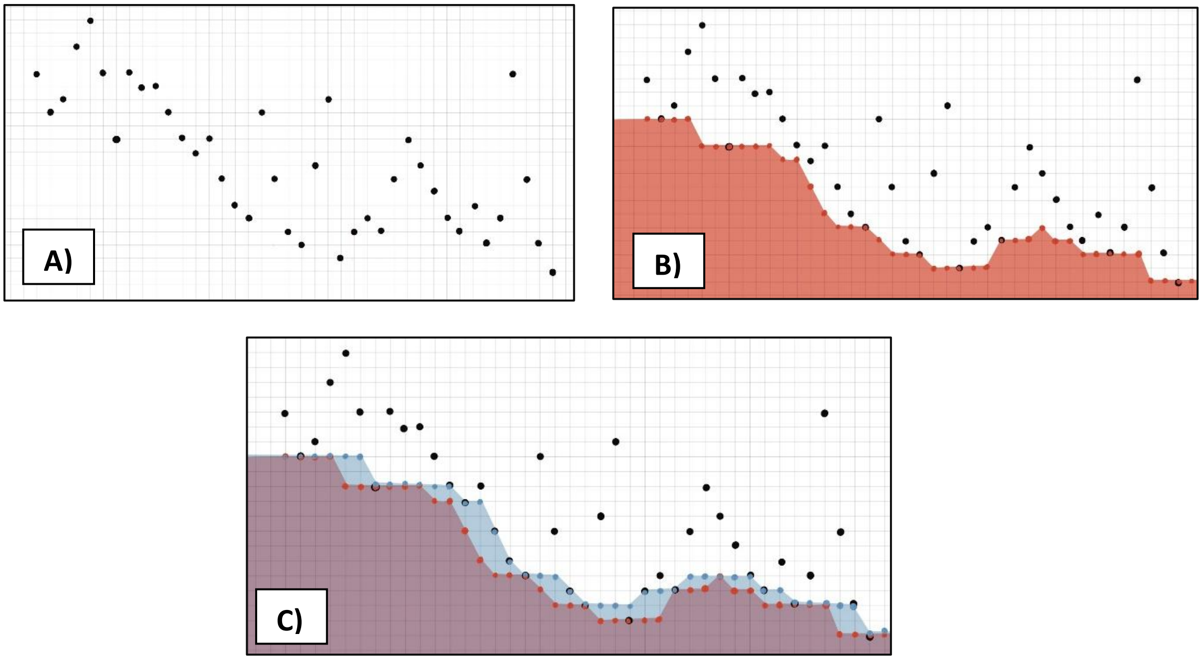

Figure 4.6 A hypothetical dataset displaying the application of a five-point running minimum and maximum filter. A) the hypothetical dataset with no filter. B) The five-point running minimum filter results are displayed in red. C) The five-point running maximum filter results are displayed in blue, overlaid on top of the running minimum filter results.

the window remains small, the filter will process a narrower depth range within the larger dataset at each step capturing too many short-term variations. Conversely, an excessively large window smooths the data too much, obscuring short-lived but significant patterns.

To address the window size, one of the Argo float datasets used by Briggs et al. (2020) was analyzed. The float data was obtained through the Argo Global Data Assembly Center in Brest France (ftp://ftp.ifremer.fr/ifremer/argo/dac/coriolis) and came from Argo float WMO Number 6901523.

The optical data collected per meter was calculated for the Argo float and glider datasets. The Argo float profiles had an average of 0.726 points/m, and the gliders had an average of 2.83 points/m. The gilder had an average of 3.9 times more data than the Argo floats. Based on this ratio, the 11-point window was scaled to a 43-point to accommodate the increased data density.

This filtering approach effectively isolated b_{bs} while retaining broader trends. By scaling the window size to account for the higher data density of gliders, the method maintained consistency with the previous Argo float study.

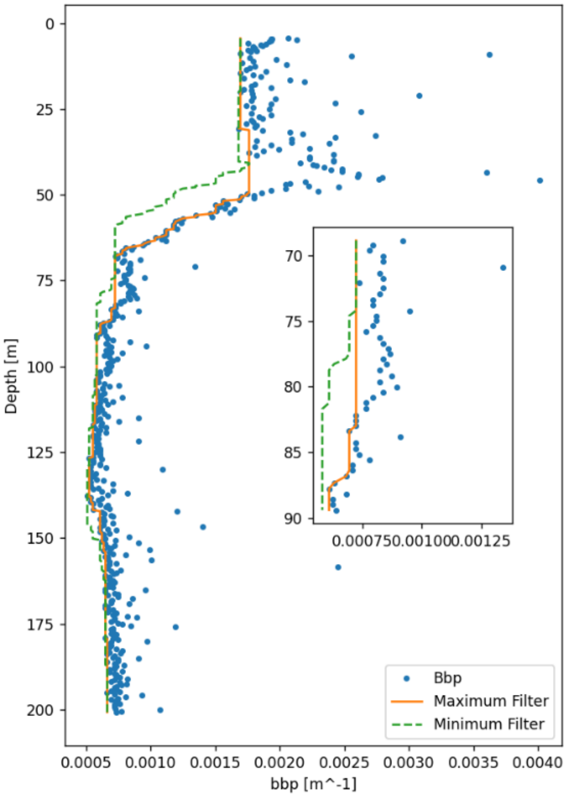

Figure 4.7 An example depth (m) profile comparing b_{bp} (m^{-1}) to the 43-point running minimum and maximum filters. The profile was collected on August 23rd, 2023, from 11:44 to 13:14 UTC. The profile began at 48° 53' 53.32" N and 130° 40' 51.70" W.

4.3.2 Estimation of Instrument Noise (b_{br})

Ideally, deep casts (depths >200 m) are used to estimate instrument noise (b_{br}), as they contain minimal particulate matter and provide a more accurate representation of noise. However, the glider deployment only included two deep casts with optical backscatter data.

Most profiles reached depths close to or below 200 m, so backscatter data from depths >180 m were used instead to estimate the noise.

For each profile, we averaged and compiled the backscatter values at depths >180 m into a new dataset of averages (black lines in Figure 4.8). The median of these averages was calculated, and profiles with an average that exceeded twice the median were removed (blue lines in Figure 4.8). We repeated this process, and the final median (6.12e^{-5} m^{-1}) was used as the instrument noise (Orange dashed line in Figure 4.8). The removed profiles were spread across the glider mission, with a few clustered spots. These clusters were likely areas with enhanced particle matter at depth, raising the averages in the area. There is also a gap in the averages (Figure 4.8), which is an area where profiles were removed due to sensor saturation.

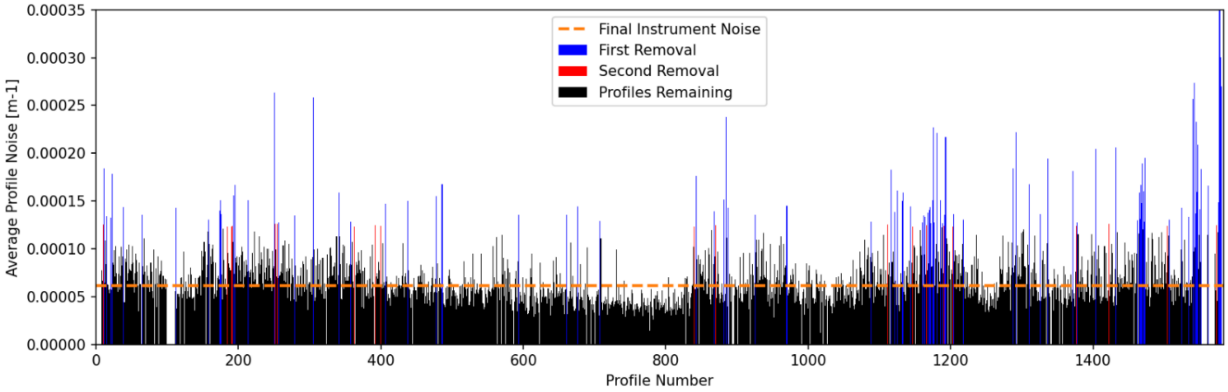

Figure 4.8. Average backscatter at depths greater than 180m for glider profiles along Line P. The blue lines represent the averages that were removed during the first pass as they were greater than two times the median of all the averages. The red lines were removed in the second pass and the black lines are what was left after the removals. The orange dashed line is the final median and estimated instrument noise.

To validate this estimate, we compared it to the two available deep casts. The backscatter averages for these profiles at depths >200 m were 7.06e^{-5} m^{-1} and 7.02 e^{-5} m^{-1}. These slightly higher values may reflect the inclusion of larger particle signals, as the limited number of deep casts prevented the application of the same outlier removal process. Nevertheless, the estimated noise of 6.12e^{-5} m^{-1} was deemed accurate for subsequent calculations, as it closely aligns with the deep-profile values and falls within the range reported by Briggs et al. (2020), where some sensors exhibited noise levels up to 6.2e^{-5} m^{-1}.

4.3.3 Isolating Optical Backscattering from Large Particles (b_{bl})

Once b_{br} and b_{bs} were separated, they could be subtracted from the total b_{bp} to get b_{bl}, the optical backscattering coefficient due to large particles. The comparison between large and small particles is the primary focus of our analysis and is compared to chlorophyll to observe productivity patterns along Line P. We display a few of the processed profiles in Figures 4.9-4.13 comparing b_{bp} (black line), b_{bs} (green line), b_{br} (red line), and b_{bl} (blue line).

We want to emphasize that the backscatter profiles exhibit distinct behaviors across these figures and throughout the extent of the mission. There's an interesting difference between Figures 4.9 and 4.10 compared to the later three figures. In Figures 4.11, 4.12 and 4.13 the separation of small and large scattering is clear because the spikes are localized and smaller. Whereas in Figures 4.9 and 4.10, we observe a few broad, intense spikes that span a large range of depths. These broad spikes and the flattened b_{bs} pattern across them (Figure 4.9), suggest that some scattering from a high concentration of smaller particles is being misattributed as large aggregates. This discrepancy could be due to the window size used in the minimum and maximum filters, and this should be addressed in future research.

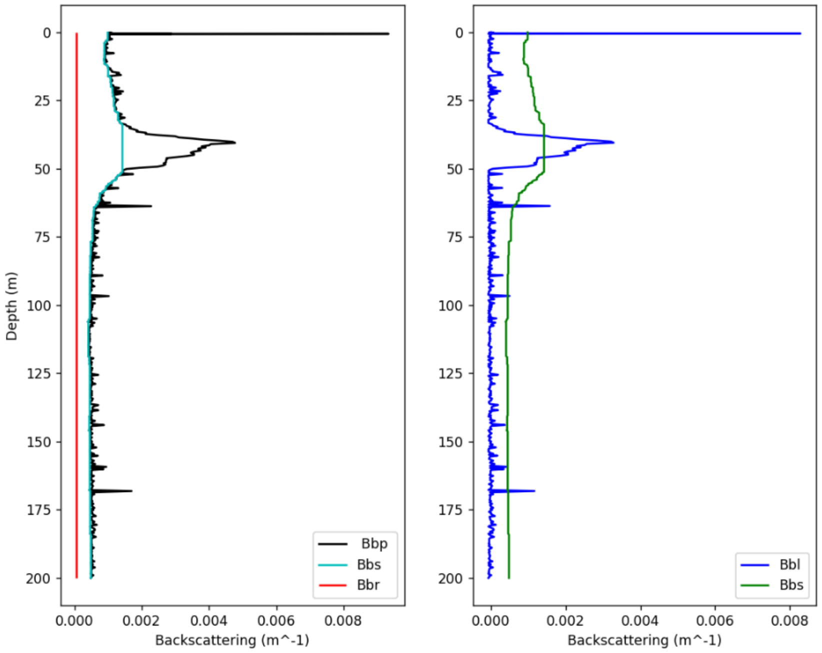

Figure 4.9 A depth (m) profile comparing the total particulate backscattering coefficient (b_{bp} m^{-1}; black line) with the backscattering due to instrument noise (b_{br} m^{-1}; red line) and small, labile particles (b_{bs} m^{-1}; cyan line)) is shown on the left. On the right is the same depth profile comparing the particulate backscattering due to large (b_{bl} m^{-1}; blue line)) and small (b_{bs} m^{-1}; green line) particles. The profile was collected on 12 Aug 2023, from 18:12 to 19:49 UTC. The profile began at 48° 39' 39.53" N and 127° 20' 39.02" W.

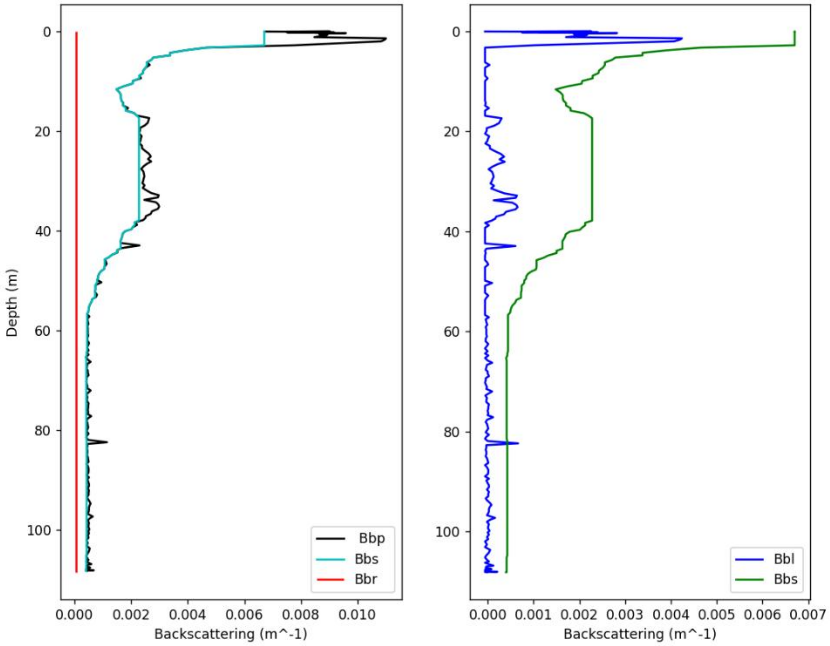

Figure 4.10 Same as Figure 6.9 except the profile was collected on 11 Aug 2023, from 1:42 to 1:50 UTC. The profile began at 48° 38' 51.33"N and 126° 37' 48.66" W.

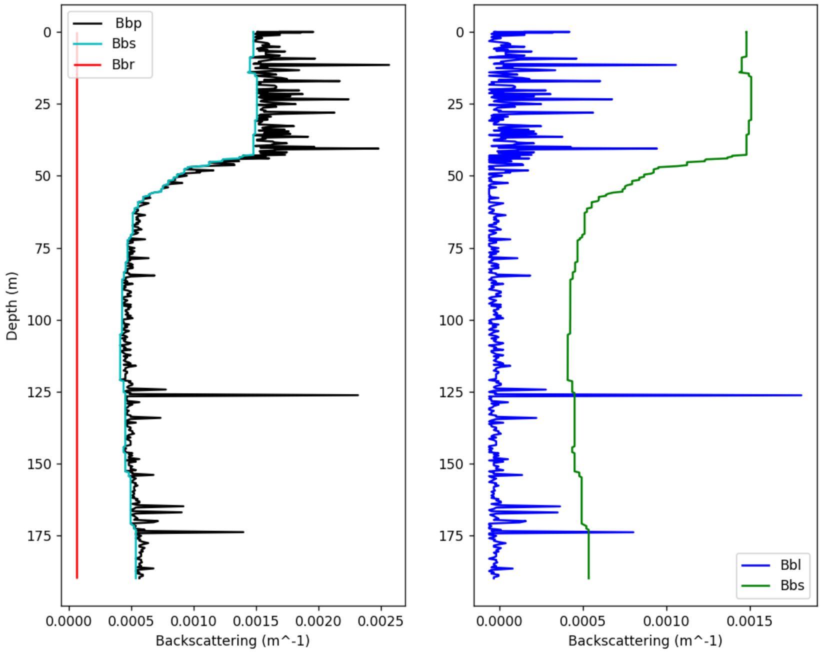

Figure 4.11 Same as Figure 6.9 except the profile was collected on 16 Oct 2023, at 22:49 UTC to 17 Oct 2023, at 4:00 UTC. The profile began at 49° 36' 0.37"N and 138° 58' 5.28" W.

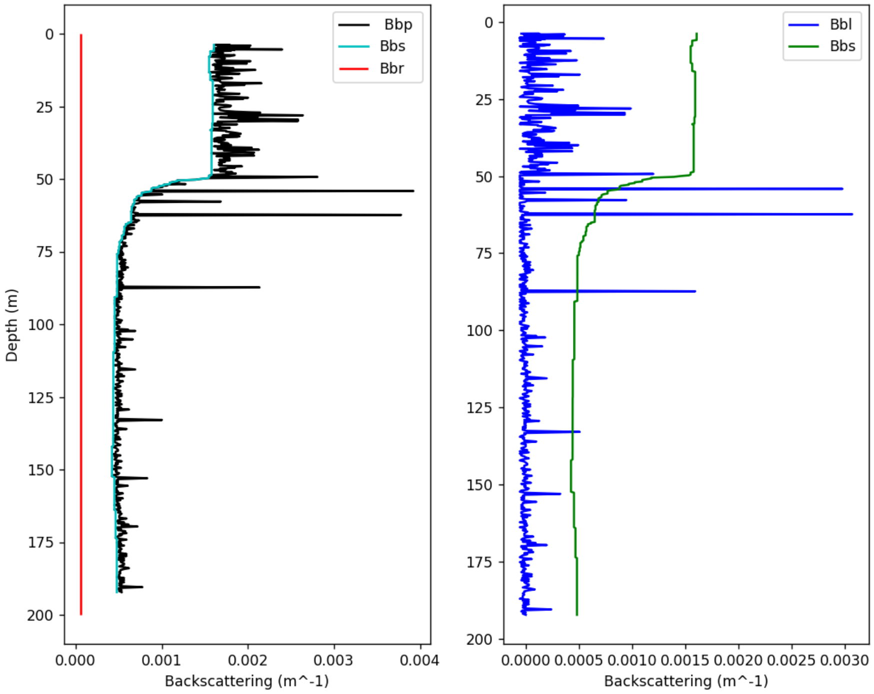

Figure 4.12 Same as Figure 6.9 except the profile was collected on 10 Oct 2023, from 13:17 to 14:52 UTC. The profile began at 4 49° 45' 55.99" N and 141° 32' 33.99"W.

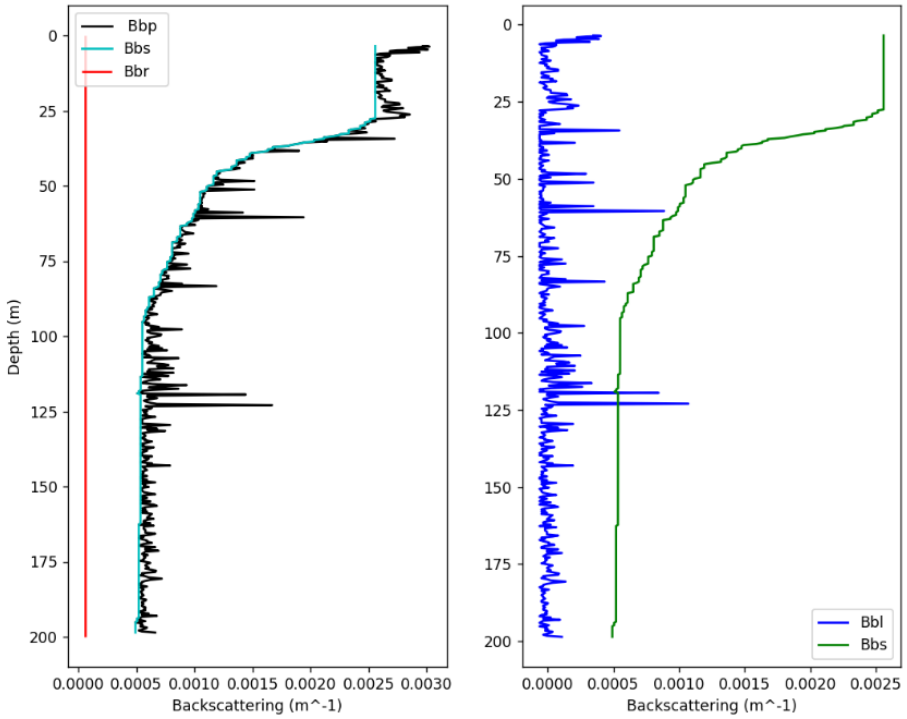

Figure 4.13 Same as Figure 6.9 except the profile was collected on 31 Aug 2023, from 14:31 to 16:06 UTC. The profile began at 49° 13' 14.5842" N and 133° 38' 35.2602" W.

4.4 Additional Processing

For visualization purposes, we estimated the mixed layer depth (MLD) using a fixed density threshold of 1024.5 kg m^{-3} across all profiles along Line P. This threshold was selected by first visualizing the glider's density colormap, then choosing a density value that aligned well with the observed density transition. The estimated MLD was then plotted on the density colormap to confirm consistency. While MLD varies due to local stratification and temporal changes, this approach provided a simple, consistent reference for depth-longitude transect plots. This estimate is not intended as a precise MLD determination but serves as a visual aid to contextualize particle distributions.

The dataset was originally not gridded, making visualization challenging. To analyze depth and longitude patterns in particulate backscattering and chlorophyll, we applied a 2D binning approach. Longitude and depth were divided into 200 and 500 bins, respectively, with the mean value of each parameter computed within each bin. On average, each longitude bin contained approximately eight profiles, and each depth bin covered around 0.4 meters. The binned data is visualized using color-mapped profiles, with mixed layer depth contours overlaid for context. For higher-resolution zoomed-in plots, the bin number was increased.

4.5 Ancillary Data

Combined Bathymetry - topography data was used to create the map of the study location (Figure 4.1). The data is from GEBCO's current gridded bathymetric data set, the GEBCO_2024 Grid (DOI: 10.5285/1c44ce99-0a0d-5f4f-e063-7086abc0ea0f). Information on the development of the data set and the source data sets included in the grid can be found in the data set documentation on https://www.gebco.net. The raw data was plotted, but no additional processing was conducted.

Sea surface anomaly satellite data is used in this study's method application. The data used E.U. Copernicus Marine Service Information: Global Ocean Gridded L4 Sea Surface Heights and Derived Variables Reprocessed 1993-Ongoing (DOI: 10.48670/moi-00148). The “Daily” data was downloaded for 26 and 19 Aug 2023 as well as 02 Nov 2023 and 26 Oct 2023. The raw data was plotted, but no additional processing was conducted.

Satellite chlorophyll concentration data is used in this study's method application. The data was obtained from GlobColour (http://www.globcolour.info). 8-day merged MODIS/VIIRSN

(GSM method) data for 24 – 31 Oct 2023 and 21 – 28 Aug 2023 was obtained, and the raw data was plotted with no additional processing.

The satellite sea surface temperature data used in this study's method application was obtained from NOAA National Centers for Environmental Information. The NOAA 0.25-degree Daily Optimum Interpolation Sea Surface Temperature V2-AVHRR Daily data for 29 Oct 2023 was used (Huang et al., 2020; DOI: https://doi.org/10.25921/RE9P-PT57) The raw data was plotted with no additional processing.

5. Method Application

In this section, I present the application of our processing method on optical backscatter data alongside the chlorophyll fluorescence measurements collected during the Line P glider mission. These datasets offer critical insights into the distribution of particles and phytoplankton, which are essential for understanding carbon cycling and transport in the ocean (Claustre et al., 2021). The primary goal of this study was to develop an algorithm for processing optical backscatter data from autonomous gliders, allowing for improved characterization of particle size distributions. The example presented here demonstrates the effectiveness of this approach in identifying biologically and physically driven patterns in the upper ocean.

Particle and phytoplankton distributions along the glider's outbound and return journey to Ocean Station Papa show variations with depth and location, reflecting the dynamic nature of the water column throughout the mission. In the following analysis, I will examine several key features revealed in the data processed by our algorithm (Figures 5.1 & 5.2), including:

1. The subsurface chlorophyll maximum, where particle concentrations align with phytoplankton distributions (Figure 5.1)
2. A nepheloid layer on the continental slope, indicating areas of enhanced sediment resuspension.
3. A high-productivity area in the mixed layer during August and November (Figure 5.2)
4. Distinct regions dominated by different particle size classes, offering insight into particle export and carbon sequestration (Figures 5.1 & 5.2)

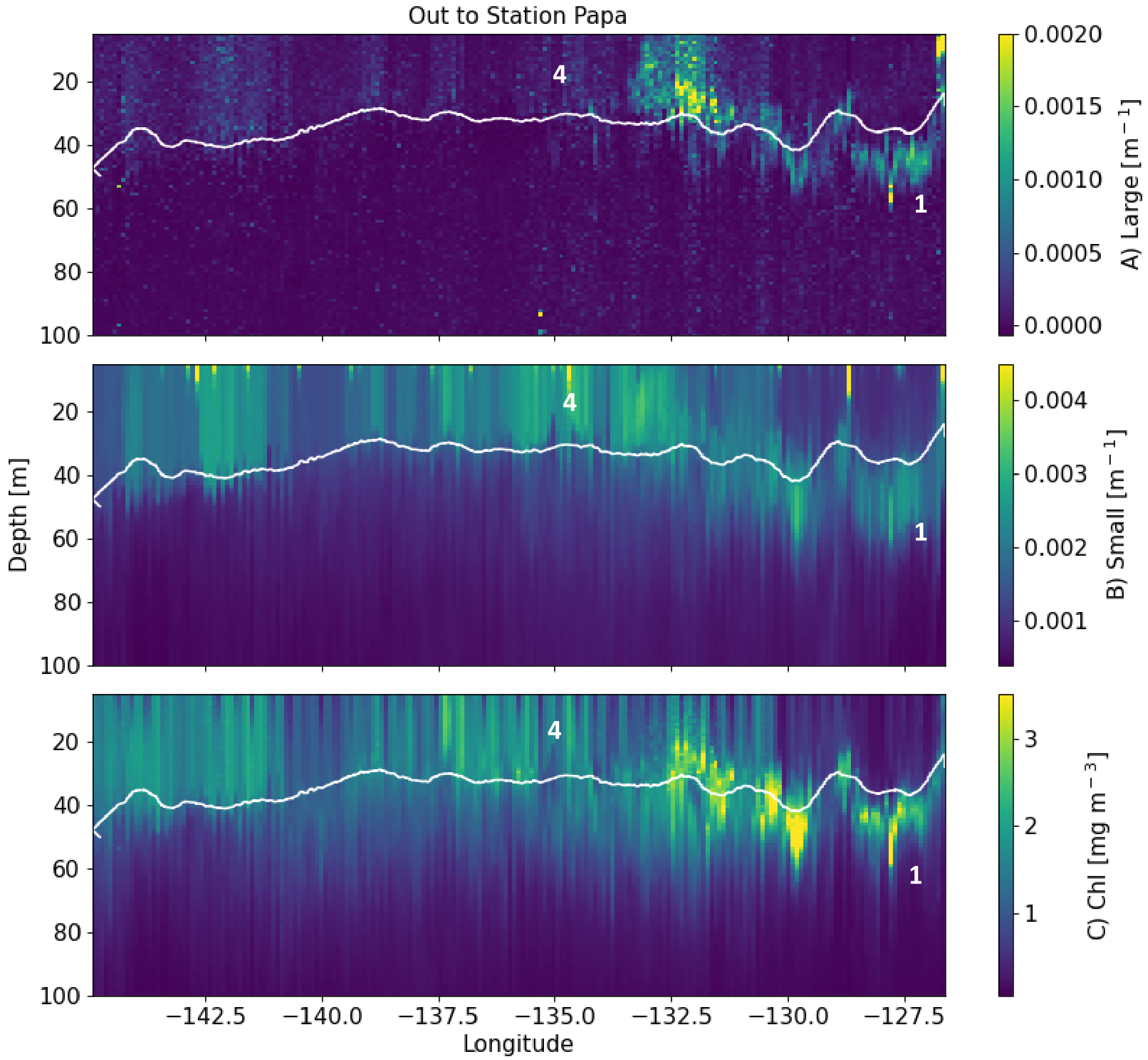

Figure 5.1 Depth (m) – Longitude transects along Line P for the trip to Ocean Station Papa. Plot A shows large particle scattering b_{bl} (m^{-1}), B shows small particle scattering b_{bs} (m^{-1}) and C shows chlorophyll fluorescence (mg/m^3). The white line on the three plots is an estimate of the mixed layer depth. The transects display the first 100m of the water column to emphasize patterns and variability. The mission began off the coast of Tofino (right side) on 11 Aug 2023 and reached Station Papa (left side) on 1 Oct 2023. Key features have been highlighted by numbers corresponding to the list in the above discussion

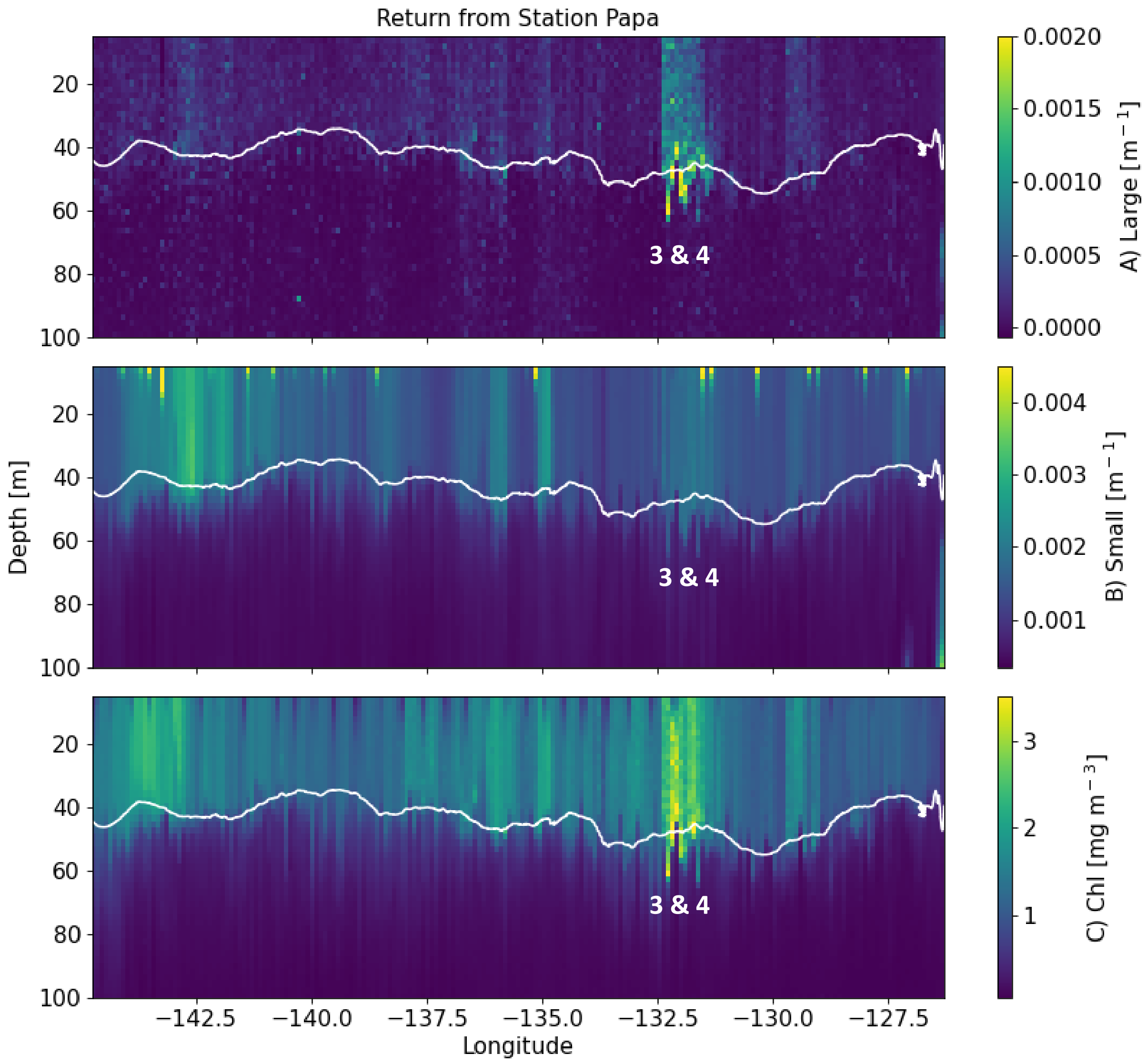

Figure 5.2 Same as Figure 5.1, except displays transects along Line P for the return from Ocean Station Papa. The return mission began at Station Papa (left side) on 1 Oct 2023 and reached the coast of Tofino (right side) on 16 Nov 2023.

5.1 Backscatter and Chlorophyll: Spearman Correlation

There is a clear visual correlation between the processed backscatter and chlorophyll data (Figures 5.1 & 5.2), suggesting a strong association between particulate matter and phytoplankton. To quantify this relationship, I performed a Spearman correlation analysis (Schober et al., 2018), which measures monotonic relationships rather than assuming linearity. This method is well-suited to oceanographic data, where biological and physical processes can produce nonlinear trends (Viljoen et al., 2024). Spearman's coefficient (ρ) ranges from -1 to 1, where values near 1 indicate a strong positive correlation (Schober et al., 2018).

In this section, I examine the relationship between optical backscatter (m^{-1}) and chlorophyll concentration (mg/m^3), first considering total backscatter (combined small and large particle contributions) before analyzing each component separately. The depth-longitude maps (Figures 5.1 & 5.2) provide spatial context, while the correlation analysis and scatter plots (Figures 5.3 & 5.4) quantify the strength of these relationships. Because chlorophyll concentrations in oceanography are typically mapped on a logarithmic scale to account for their wide dynamic range, I used a log-log scale for visualization, while statistical calculations were performed on the original scale, un-binned data.

The depth-longitude maps reveal a strong alignment between total backscatter (Figures 5.1A, 5.1B, 5.2A, & 5.2B) and chlorophyll concentrations (Figures 5.1C & 5.2C). For example, a pronounced subsurface chlorophyll maximum (Figure 5.1C) coincides with peaks in both large and small particle backscattering (Figures 5.1A & 5.1B). This pattern is further reflected in the scatterplot (Figure 5.3) and correlation analysis, which show a strong positive correlation (Spearman $\rho = 0.76$) between total backscatter and chlorophyll. These results indicate that higher backscatter values generally correspond to increased chlorophyll, reinforcing the idea that total backscatter is largely influenced by phytoplankton and their associated constituents, such as zooplankton and detrital matter. (Brewin et al., 2012).

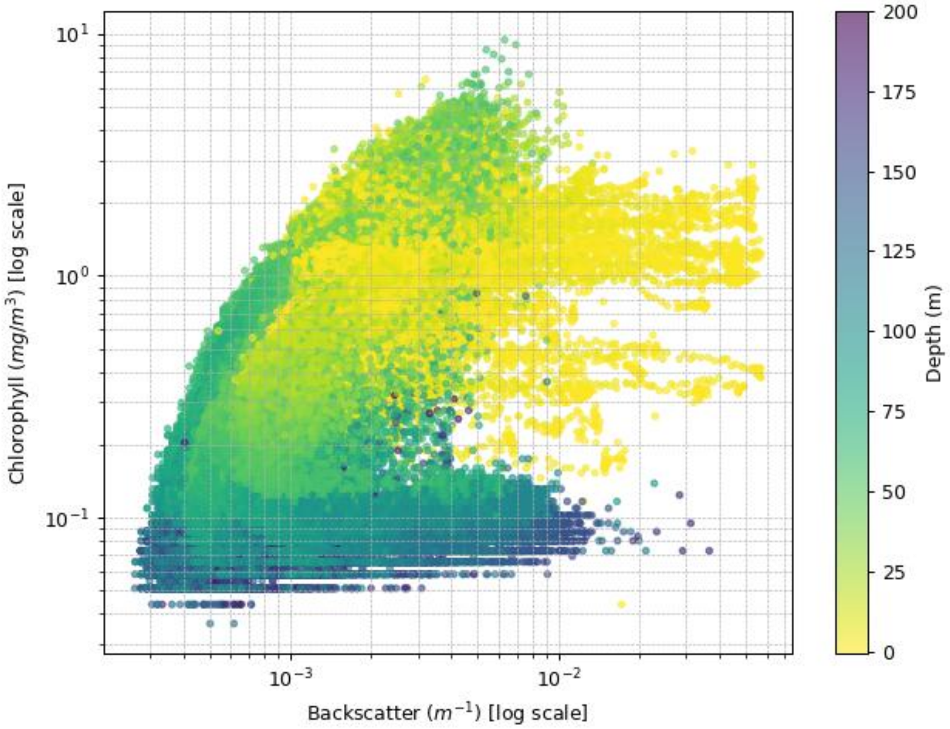

Figure 5.3 Correlation plot between combined backscatter (b_{bs} + b_{bl}) and chlorophyll concentration (mg/m^3) with a depth (m) colour bar. Both backscatter and chlorophyll are on a log scale.

By breaking down total backscatter into its small- and large-particle components (Figure 5.4), we uncovered significant differences in their relationships to chlorophyll. Small-particle backscatter (b_{bs}) exhibits a strong correlation with chlorophyll (ρ = 0.79), while large-particle backscatter (b_{bl}) shows a much weaker association (ρ = 0.19).

These findings align with the spatial patterns observed in the depth-longitude maps (Figures 5.1 & 5.2). b_{bs} visually follows the chlorophyll distribution, reinforcing the idea that it predominantly represents phytoplankton particles and byproducts. In contrast, b_{bl} is more spatially sporadic and does not consistently align with chlorophyll distribution. Instead, b_{bl} appears more prominent in distinct regions, and likely depends on additional processes such as zooplankton, aggregation and fragmentation (Clements et al., 2022).

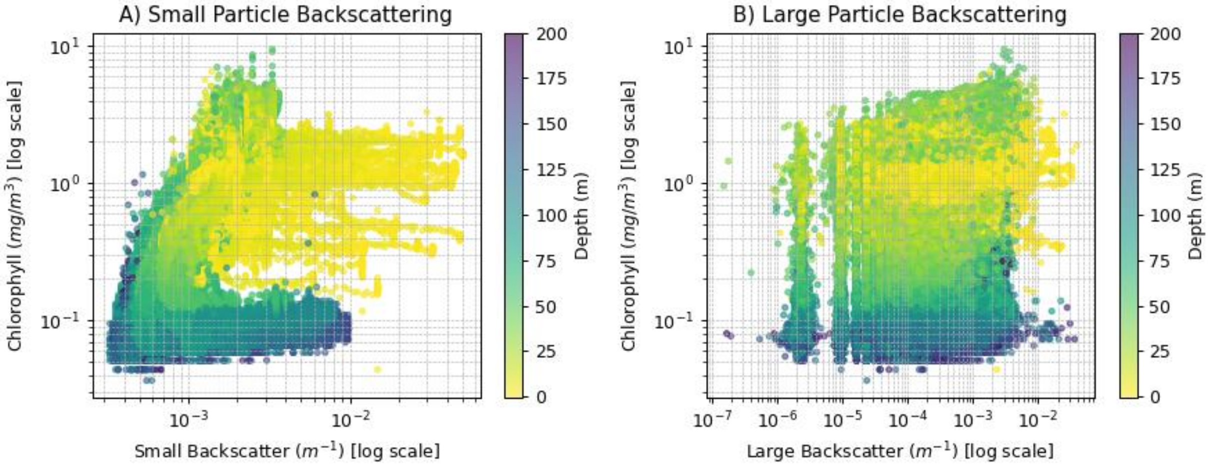

Figure 5.4 Correlation plots between small particle b_{bs} (A) and large particle b_{bl} (B) backscatter and chlorophyll concentration (mg/m^3) with a depth (m) colour bar. Both backscatter and chlorophyll are on a log scale.

The weak correlation between large-particle backscatter and chlorophyll highlights the necessity of distinguishing between different size classes when interpreting backscatter data. If we were to analyze only total backscatter, we might misattribute signals, such as some aggregates, detritus, or resuspended sediments, as biological productivity. By separately examining small- and large-particle contributions, we can better differentiate phytoplankton-driven backscatter from other sources, leading to more accurate interpretations of oceanographic optical data.

The color gradient in the correlation plots (Figures 5.3 & 5.4), representing depth, highlights a clear vertical structure in the relationship. At shallower depths (yellow) both chlorophyll and backscatter values are consistently high, aligning with expected phytoplankton distributions in the upper mixed layer. In contrast, deeper waters (purple) show consistently lower chlorophyll concentrations, while particle backscatter (especially b_{bl}, Figure 5.4B) varies more widely. This suggests that the deeper surface backscatter signals may be influenced by non-phytoplankton sources, such as particle aggregation, zooplankton, or transport, rather than direct biological production.

It is important to note that chlorophyll fluorescence is subject to quenching by sunlight, which reduces the observed fluorescence signal, particularly in the top 25 meters of the water column during daylight hours (Sackmann et al., 2008; Thomalla et al., 2017). This quenching effect, visible as striped patterns in Figures 5.1C and 5.2C, likely altered our results by underestimating some of the fluorescence signals (Thomalla et al., 2017). Consequently, the correlation between chlorophyll and backscatter may be weakened, especially during the day. A more accurate future analysis would exclude daytime values, focusing solely on nighttime data when fluorescence measurements are unaffected by sunlight. Additionally, a future focus of this work could be to separately examine signals from the mixed layer, the chlorophyll maximum, and deeper waters, to better understand how each area contributes to the overall relationship between chlorophyll and backscatter.

5.2 Subsurface Chlorophyll Maximum & Particle Distribution

The subsurface chlorophyll maximum (SCM) is a prominent feature in our study region, evident in the depth profiles of chlorophyll and backscatter (Figure 5.1, labelled as 1). These layers, where chlorophyll concentrations exceed those of surface waters (Richardson & Bendtsen, 2019), play a significant role in regional primary productivity (Anderson, 1969) and are therefore crucial for understanding the export of particulate organic carbon in the area. In this section, we explore the nature of the SCM observed during the glider mission, focusing on its depth, the association between chlorophyll and particle backscatter, and the biological processes that drive this relationship.

Subsurface chlorophyll maxima (SCM) are layers where chlorophyll concentration is significantly higher than in surface waters (Richardson & Bendtsen, 2019). In our study area, we observed the SCM during the outbound leg of the glider mission near the coast (between Line P stations P5 to P15) from approximately 127° W to 133° W, in mid to late August 2023. The SCM was found at depths of approximately 30 to 60 meters, just beneath and above the mixed layer depth (MLD). This depth and timing align with typical SCMs in temperate regions like the Northeast Pacific, where they occur from late spring to summer (Ross et al., 2017). However, we would expect the SCM to be entirely below the mixed layer, but this discrepancy may be due to how we estimated the MLD.

There are two main types of SCMs. The first type, often found in subtropical regions or highly stratified waters, occurs at greater depths (>100 meters). In these areas, the water column is highly stratified, and nutrients are only found deeper in the water (Perry et al., 2008). Phytoplankton in these regions adapt to low light by increasing their chlorophyll-a content per cell, enhancing light capture at depth (Masuda et al., 2021). Thus, the chlorophyll maximum reflects higher chlorophyll production rather than a biomass peak (Martin et al., 2010) For this reason, the chlorophyll peak in these areas is often deeper than the particle peak, meaning that optical backscatter measurements do not show an increase at the same depth (Martin et al., 2010). However, this is not the case in our study area, where the chlorophyll peak occurs at a shallower depth, and the particle peak (measured by backscatter) aligns with the chlorophyll peak (Figure 5.5).

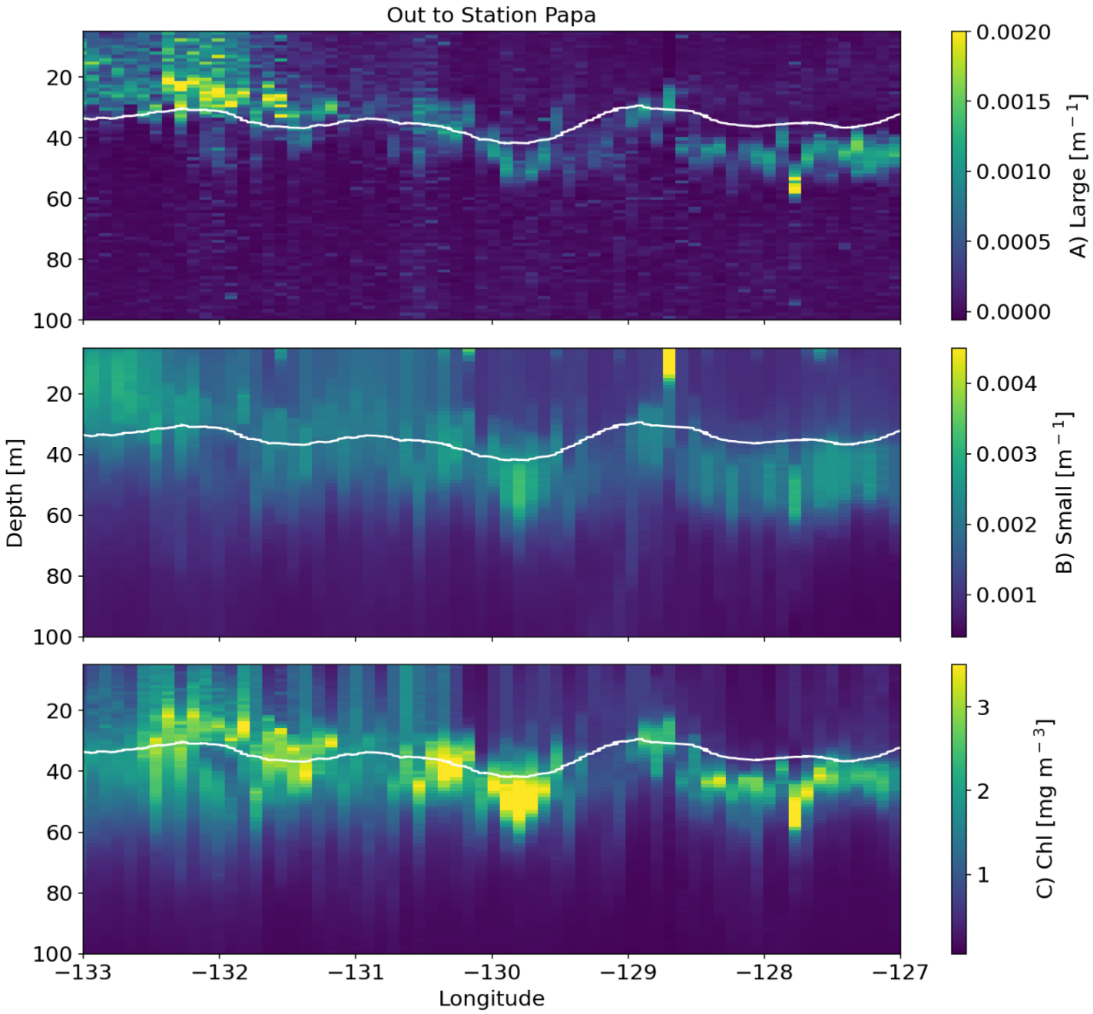

Figure 5.5 Subset of Figure 5.1, limited to the data from 133° W to 127° W, highlighting a backscatter and chlorophyll fluorescence peak. The subset of the glider mission occurred from 11 Aug to 29 Aug 2023.

The second type of SCM, more common in temperate waters like our study area, form when a previous phytoplankton bloom has depleted the nutrients from the surface waters and occur at shallower (~50 meters) depths (Anderson, 1969). The phytoplankton concentrations decrease with the nutrient depletion, allowing light to penetrate deeper into the water column (Perry et al., 2008). This increased penetration of light allows phytoplankton to grow at a deeper depth where nutrients are present, forming the SCM (Richardson & Bendtsen, 2019). In these cases, the chlorophyll maximum is aligned with the particle maximum, meaning that both chlorophyll and backscatter measurements show peaks at the same depth (Perry et al., 2008). This is exactly what we observed in our study area, where the shallow chlorophyll maximum coincided with large and small particle backscatter peaks at the same depth (Figure 5.5). This suggests that the SCM in our region is likely controlled more by nutrient depletion at the surface rather than strong stratification and low light availability (Martin et al., 2010). This would also explain why the SCM is absent farther along the line, in a major high-nitrate, low-chlorophyll (HNLC) zone where productivity is limited by iron availability rather than macronutrient supply (Zhang et al., 2021).

Notably, this SCM was only present during the glider mission in August and was no longer observed in November. In the fall, the water column undergoes destratification, leading to the mixing of phytoplankton from the subsurface layers to the surface disrupting the SCM (Perry et al., 2008). This highlights the seasonality of subsurface chlorophyll maximums in temperate regions.

5.3 Nepheloid Layer on the Continental Slope

A pronounced spike in both large and small particle backscatter signals near the seafloor was observed, initially suggesting the presence of a high-productivity zone (Figure 5.6). However, the absence of a corresponding chlorophyll signal, combined with the depth of this spike, led us to a different interpretation.

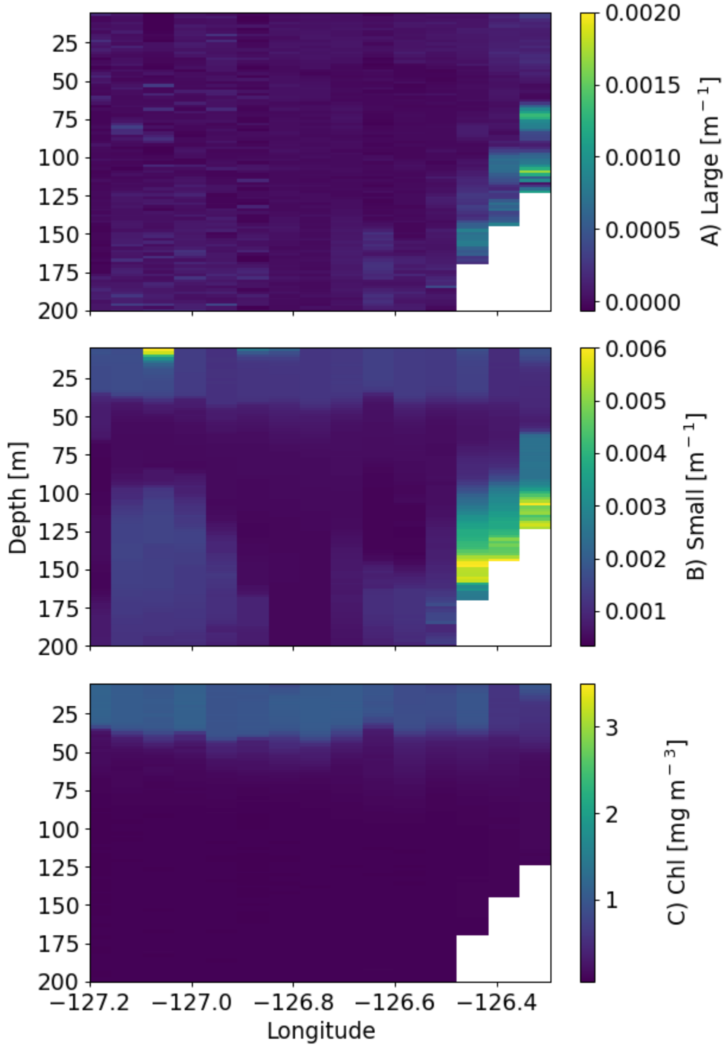

Figure 5.6 Subset of Figure 5.2, showing data from 127.2° W to 126.30° W and extending to a depth of 200m. This plot displays backscatter and chlorophyll data along the continental slope from 15 Nov to 16 Nov 2023. The white areas indicate regions where data was not collected due to the glider reaching the sea floor.

The location along the continental slope suggested that this feature is more likely a nepheloid layer, where sediment resuspension drives elevated particle concentrations (Puig et al., 2022; Ye et al., 2024). The depth of the backscatter spike (>75m) suggests that photosynthetically active radiation (PAR) at this depth is likely insufficient to support significant phytoplankton growth, especially in coastal environments with higher turbidity or sediment resuspension (Wang et al., 2019). This is further supported by the lack of chlorophyll signals, indicating that the particles are not linked to primary production. Instead, the observed increase in particle backscatter is likely due to local ocean currents, turbulence, and seafloor interactions which resuspend sediments and enhance the particle concentration in this region (Durrieu de Madron et al.,2017). While not directly related to the core focus of our study, this observation highlights an interesting dynamic in the cross-shelf particle distribution and suggests other applications for glider-based optical backscatter analysis.

5.4 High-Productivity Area Investigation

A high-chlorophyll patch was observed near 132° W during both the outbound and return legs of the glider mission (Figures 5.1C and 5.2C). The initial spike was captured on 26 August 2023. Unexpectedly, a similar increase was captured on 2 November 2023, when the glider passed the same location. The November spike was unexpected for this time of year as phytoplankton concentrations typically decrease during the fall as surface waters cool and light availability is lowered. Both events coincided with high backscatter, suggesting elevated particulate matter concentrations, particularly large aggregate spikes (Figures 5.7 and 5.8).

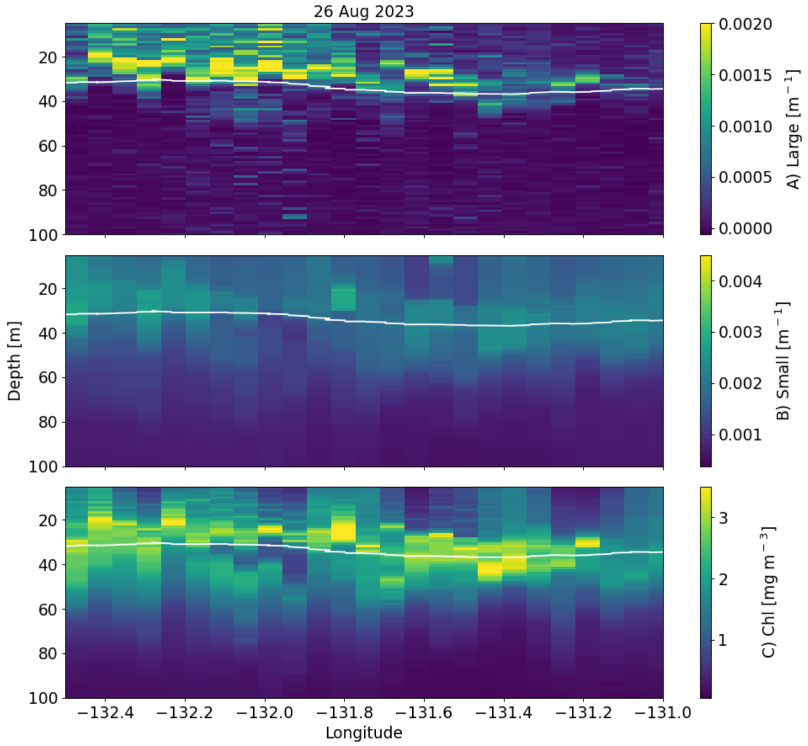

Figure 5.7 Subset of Figure 5.1, showing data from 132.5° W to 131.0° W, highlighting a spike in chlorophyll and backscatter data on 26 Aug 2023

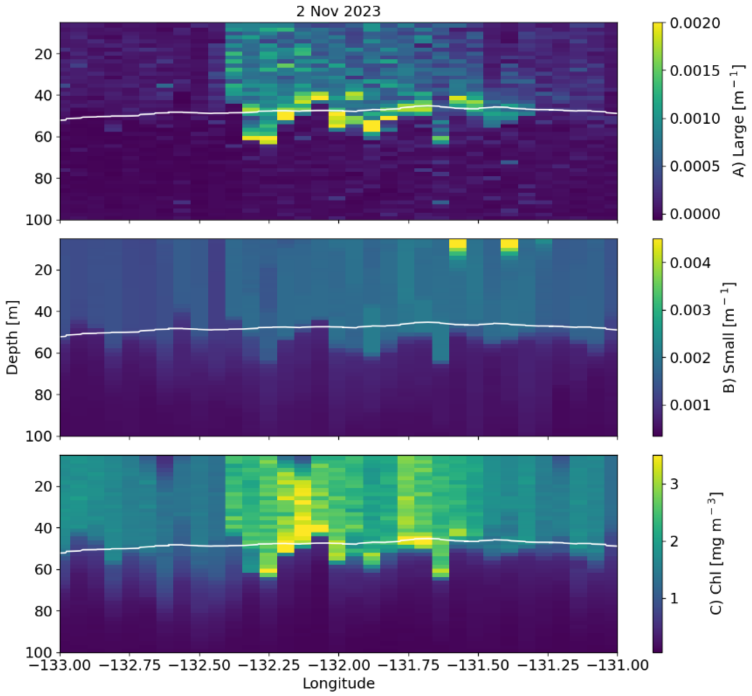

Figure 5.8 Subset of Figure 5.2, showing data from 133° W to 131.0° W, highlighting a spike in chlorophyll and backscatter data on 2 Nov 2023.

No eddy influence was detected during either event, as no significant sea surface height (SSH) anomalies were observed before or during the time frame they occurred (Figures 5.9 & 5.10). Sustained productivity and elevated chlorophyll in this region are often linked to anticyclonic eddies, which drive iron and nutrients to the surface (Crawford et al., 2005; Crawford et al., 2007). We initially hypothesized that these eddies were responsible for the observed chlorophyll and backscatter spikes (Figures 5.7 & 5.8). However, the absence of a significant rise in sea surface height suggests that an eddy did not influence this event.

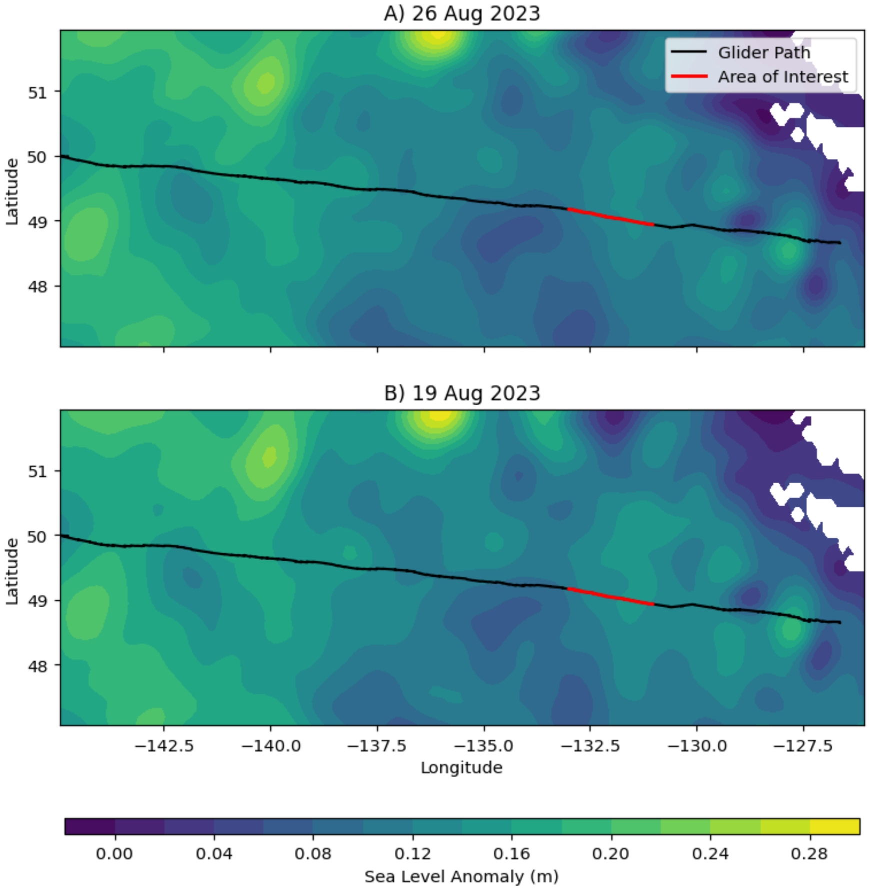

Figure 5.9 Satellite sea surface height anomalies (m) along the outbound glider track. The black line shows the path the glider followed with the high chlorophyll event highlighted in red. Satellite data from E.U. Copernicus Marine Service Information (Global Ocean Gridded L4 Sea Surface Heights). The daily satellite data is shown for A) 26 Aug 2023 and B) 19 Aug 2023.

.

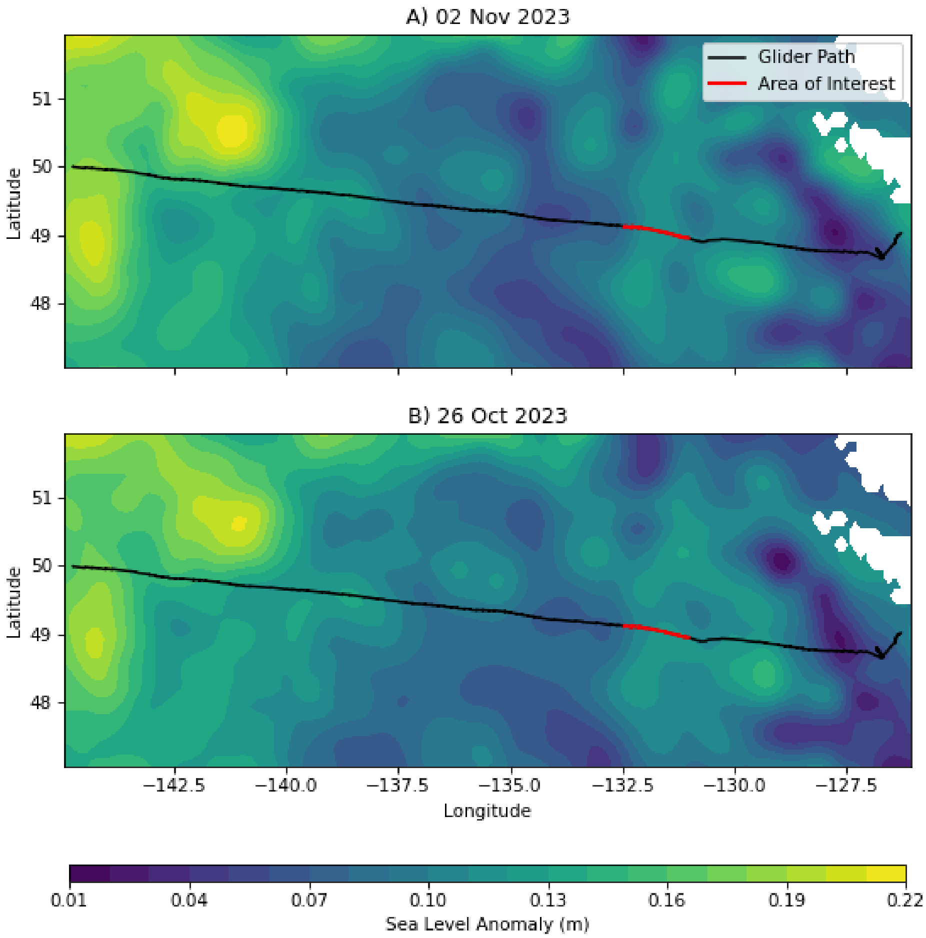

Figure 5.10 Same as Figure 5.9 except the daily satellite data is shown for the return glider track on A) 02 Nov 2023 and B) 16 Oct 2023.

No significant anomalies were observed in temperature, salinity, or density profiles from the glider mission, suggesting that physical forcings such as localized mixing or upwelling did not cause the event. In particular, the seasonal pycnocline in the study area did not show signs of being shallower or deeper than in adjacent locations, which would typically indicate the presence of an eddy (Crawford et al., 2007).

Satellite-derived chlorophyll concentrations confirmed the presence of elevated chlorophyll in the region, although with some limitations in data availability. Due to cloud cover, only the 8-day composite before the November event was available, but it did show elevated surface chlorophyll in the area (Figure 5.11). The August event was not as prominent in the satellite data (Figure 5.12), likely because it was a subsurface peak, which would be less visible from space due to the shallower optical depth of satellite sensors compared to the depth of the detected subsurface chlorophyll maximum (Perry et al., 2008).

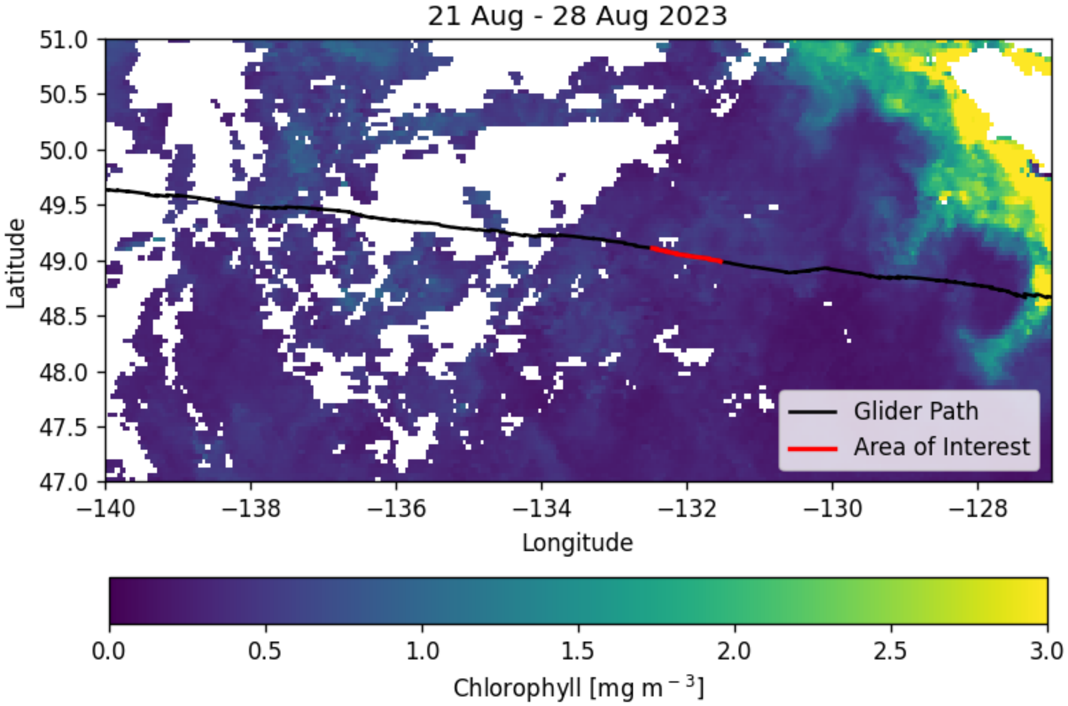

Figure 5.11 Satellite chlorophyll concentrations (mg/m^3) along the outbound glider track. The black line shows the path the glider followed with the high chlorophyll event highlighted in red. Satellite data from GlobColour 8-day merged MODIS/VIIRSN (GSM method) spanning 21 – 28 Aug 2023.

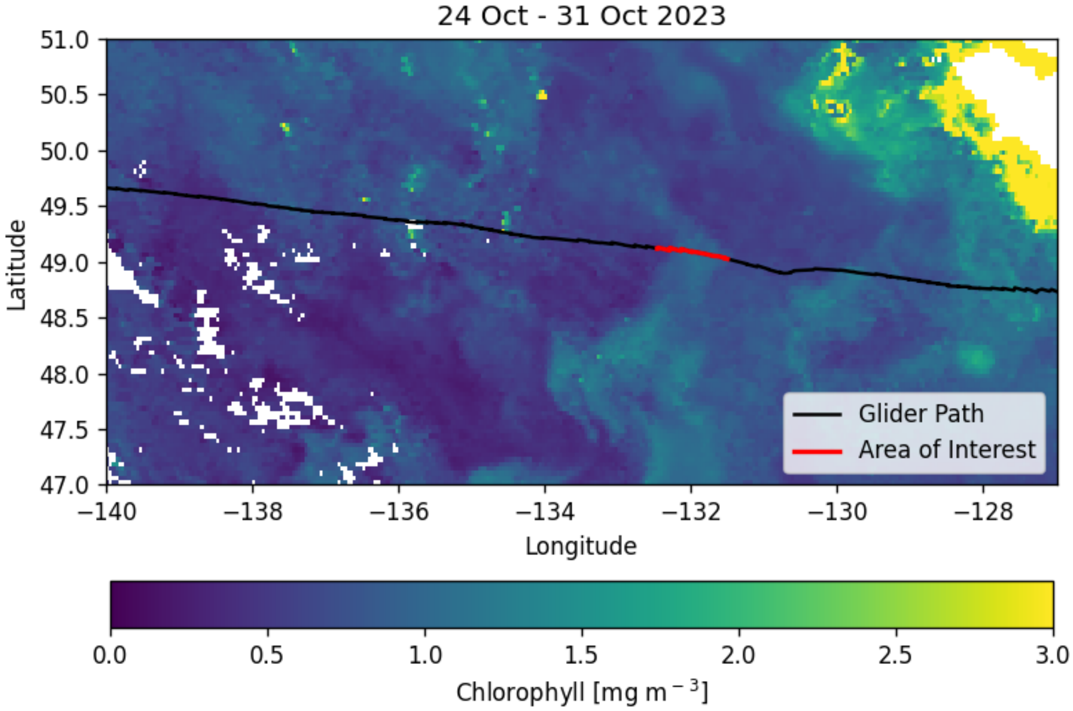

Figure 5.12 Same as Figure 5.11 except along the return glider track, spanning 24 – 31 Oct 2023.

Examination of the broader region surrounding the November high-chlorophyll anomaly, suggests it was influenced by offshore transport and large-scale circulation patterns. A high-chlorophyll filament appears to originate near 44°N, extending toward the study area (Figure 5.13A). This pattern aligns with the North Pacific circulation and may be associated with the Transition Zone Chlorophyll Front (TZCF) (Polovina, 2001), suggesting advection of chlorophyll- or nutrient-rich waters from a more distant source. Due to cloud cover, a similar analysis could not be conducted for the August event, so I focused on the November event.

The TZCF is a basin-scale feature that separates the nutrient-rich subarctic waters from the low nutrient subtropical gyre in the North Pacific (Ayers et al., 2010). It is characterized by a sharp gradient in chlorophyll concentrations and migrates seasonally, moving northward in summer (~45°N) and southward in winter (~30°N) in response to changes in temperature and circulation (Howard et al., 2010). The TZCF is a biological hotspot, where phytoplankton and zooplankton concentrate, which increases the concentration of organic particles (Polovina et al., 2001).

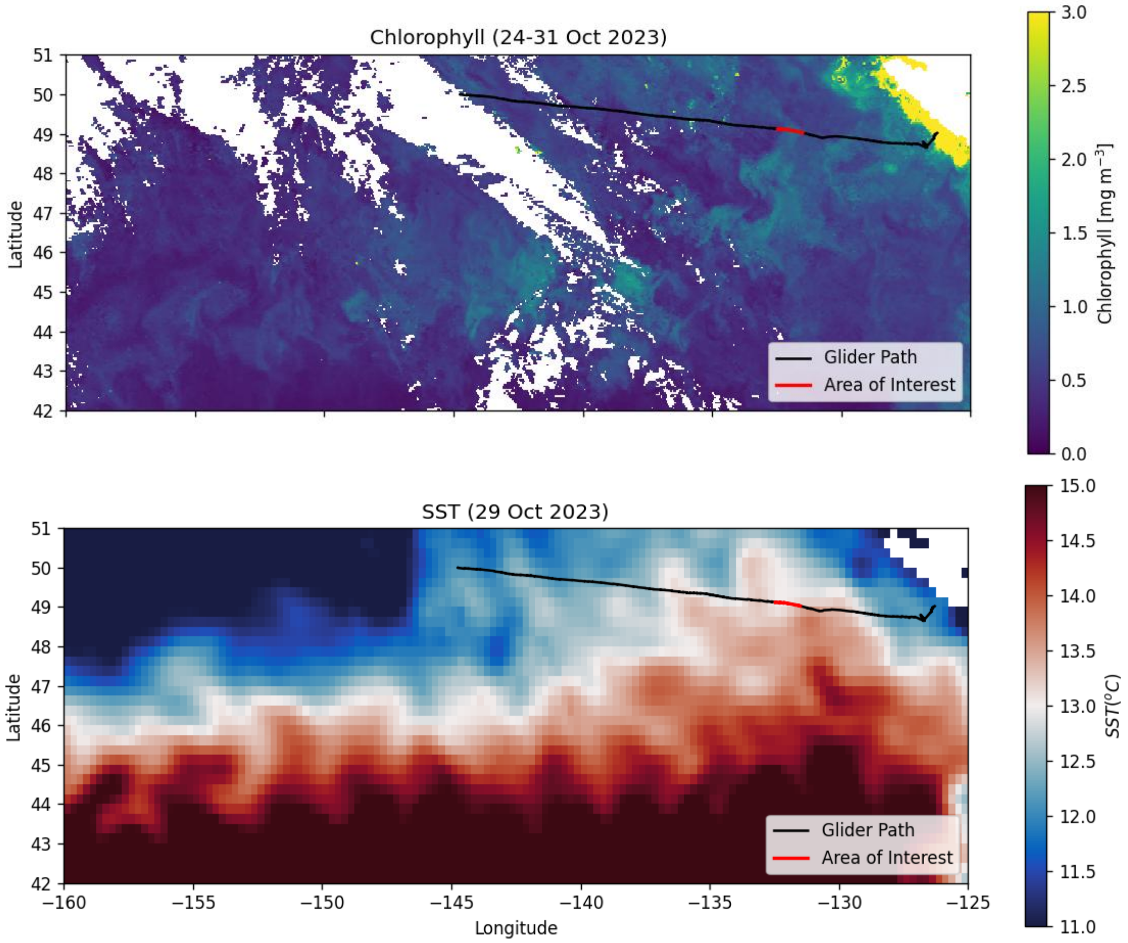

Figure 5.13 A) Expanded version of 5.11. B) Daily sea surface temperature (°C) satellite data for 29 Oct 2023. Data from NOAA (OISST Daily AVHRR-only Feature Collection/Best Time Series) The black line shows the path the glider followed with the high chlorophyll event highlighted in red.

The satellite sea surface temperature (SST) of the region reveals a convergence of two distinct water masses, creating a thermal front (~13°C). This front coincides with the high chlorophyll and particle event, with the white transitional area aligning with the highlighted red line (Figure 5.13B). This water mass convergence supports the idea that this may be connected to the TZCF. However, in November, the TZCF should have already migrated farther south than 44°N. This discrepancy may be explained by the strong El Niño event of 2023 (Raghuraman et al., 2024), which can influence the TZCF's position and intensity through changes in ocean temperatures and circulation patterns. (Polovina et al., 2001).

The precise mechanisms driving this high productivity event are still speculative and need further investigation. However, the alignment of the chlorophyll feature with the SST suggests that regional circulation patterns contributed. To fully understand the factors sustaining this productivity anomaly, it would be crucial to incorporate data on nutrient concentrations and light availability.

5.5 Regional Differences in Particle Size Distributions and Aggregation

Our analysis of optical backscatter data along Line P revealed distinct regions dominated by different particle size classes. One with high backscatter from large aggregates (Figure 5.8) and another with stronger scattering from smaller particles (Figure 5.14). Despite both regions exhibiting high chlorophyll concentrations, their differences in particle size suggest distinct variations in their carbon export efficiency. These distributions may be driven by a combination of physical forcings, biological interactions, and phytoplankton composition.

Table 5.1 Average Backscatter and Chlorophyll Concentrations in Two Contrasting Regions

Optical measurement	Units	Sept zone	Nov zone	Interpretation
Small particle backscatter (b_{bs})	m^{-1}	$2.43e^{-3}$	$2.08e^{-3}$	More small particles in Sept
Large particle backscatter (b_{bl})	m^{-1}	$7.48e^{-5}$	$7.828e^{-4}$	More large aggregates in Nov
Chlorophyll Fluorescence	$mg\ m^{-3}$	1.62	2.27	Higher productivity in Nov

The September location (Figure 5.14) had high chlorophyll (1.62 mg m^{-3}), higher small-particle backscatter (2.43×10^{-3} m^{-1}) and low large-particle backscatter (7.48×10^{-5} m^{-1}). In contrast, the November location (Figure 5.8) had slightly lower small-particle backscatter (2.08×10^{-3} m^{-1}) but a notable increase in large-particle backscatter (7.83×10^{-4} m^{-1}) and higher chlorophyll (2.27 mg m^{-3}), suggesting enhanced aggregation and potential export processes.

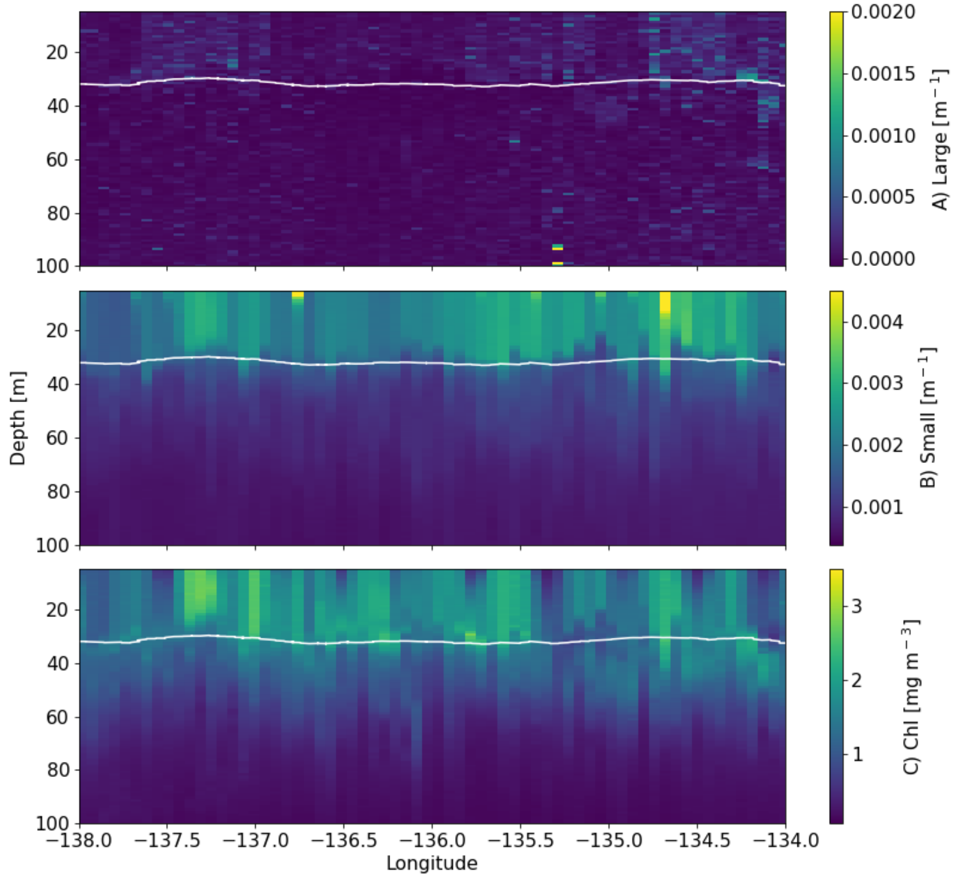

Figure 5.14 Subset of Figure 5.1, showing data from 134° W to 138° W, highlighting a spike in chlorophyll and b_{bs} with low b_{bl}. Collected on 2 - 10 Sept 2023.

The November region (Figure 5.8), characterized by higher b_{bl}, is also the high-productivity zone discussed in Section 5.4. The presence of a front may have facilitated particle aggregation through enhanced small-particle production and increased collision rates. Fronts often act as physical and biological convergence zones, concentrating particles and stimulating phytoplankton growth, both of which can elevate aggregation potential (Belkin et al., 2009). However, the role of turbulence at fronts is complex and highly variable. While moderate turbulence can promote aggregation by increasing particle collision frequency and allowing small particles to stick together (Lee et al., 2011), excessive turbulence can exert shear stress that fragments existing aggregates, keeping particles in a smaller state (Takeuchi et al., 2019). Thus, the efficiency of aggregation at fronts depends on the turbulence regime at a given time, with certain conditions favoring the formation of large aggregates and others leading to particle fragmentation.

The September region (Figure 5.14), contrasting with the November region, was dominated by smaller particles (higher b_{bs}). The enhanced November processes were potentially driven by a combination of physical dynamics, such as turbulence and frontal convergence, and biological factors, including zooplankton grazing and phytoplankton community composition. Additionally, the September region may have experienced conditions where turbulence favoured fragmentation or where reduced physical forcing limited particle interactions. The interplay between all these mechanisms ultimately shapes particle size distributions and influences carbon export efficiency. Smaller particles, with slower sinking rates, remain suspended in the upper ocean for longer periods, whereas larger aggregates are more likely to sink and contribute to deep-sea carbon sequestration (Bach et al, 2016).

Beyond physical forcings such as turbulence, biological interactions also play a key role in shaping particle distributions. Regions with higher zooplankton abundance cause increased fecal pellet production, leading to greater aggregation. Whereas areas with lower zooplankton grazing or different food sources may retain a higher proportion of smaller particles (Fischer & Karakaş, 2009). Additionally, phytoplankton composition influences aggregation dynamics. The November region may have been dominated by phytoplankton species such as diatoms, which promote the formation of larger aggregates that sink more efficiently (Briggs et al., 2011). In contrast, the September region may have had a phytoplankton community less conducive to aggregation, resulting in a dominance of smaller, more dispersed particles.

6. Conclusion

6.1 Summary

Through this research we developed an algorithm to process optical backscatter data collected by autonomous ocean gliders, tackling the challenge of distinguishing between large, fast-sinking aggregates and smaller particles. The method was adapted from the framework originally designed for Argo floats (Briggs et al., 2020), but significant modifications were necessary to account for the fundamental differences between these platforms. We demonstrated the application of this method using data from the Canadian-Pacific Robotic Ocean Observing Facility (C-PROOF) glider deployment in offshore British Columbia waters.

The method development involved several key steps: first, we reprocessed raw data to confirm measurement units and addressed sensor saturation. We then partitioned b_{bp} into three components: scattering from large aggregates (b_{bl}), smaller particles (b_{bs}), and instrument noise (b_{br}). Using a two-filter method, we isolated scattering from small particles and estimated instrument noise based on the deepest backscatter measurements. The remaining signal was attributed to large aggregates. This allowed us to effectively analyze particle size distributions and their relationship with biological productivity in the study region.

Using Spearman correlation analysis, we identified a strong correlation between small-particle backscatter and chlorophyll fluorescence, whereas large-particle backscatter was less correlated, suggesting different processes at play for each size class.

When our method was applied to the glider data, key oceanographic features such as a nepheloid layer and a subsurface chlorophyll maximum (SCM) were revealed. Additionally, the glider captured an interesting spike in chlorophyll and backscatter at the same location in August and November. After examining sea surface height anomalies alongside density, temperature and salinity transects, we ruled out eddy upwelling as the cause of this sustained productivity. Satellite chlorophyll data and sea surface temperature observations revealed a filament of increased chlorophyll that aligned with converging water masses. We hypothesize that this event may have been associated with the North Pacific circulation and the Transition Zone Chlorophyll Front (TZCF).

Finally, we examined two contrasting high-chlorophyll regions in September and November, which had significant differences in particle size distributions. The September region was dominated by smaller particles, while the November region exhibited higher concentrations of larger aggregates. These findings point to distinct variations in carbon export efficiency across the study area. We explored physical factors, such as turbulence and fronts, and biological factors, including zooplankton grazing and phytoplankton composition, to explain these variations and determined it is likely that a combination of these factors contributed to the observed patterns.

6.2 Implications

The broader implications of this method extend across several subfields of oceanography. Biologically, it offers a way to assess the distribution of organic particulate matter, helping to investigate its role in marine food webs and energy transfer. Geologically, it contributes to understanding sedimentation processes and identifying areas of resuspension. Physically, the method enhances our understanding of turbulence and mixing processes, specifically in relation to particle transport and distribution. Chemically, it provides a valuable tool for studying the transformation and sequestration of organic carbon in the water column. Most importantly, it connects these observations, helping us to better understand the interconnected processes governing the fate of atmospheric CO_2 as it enters the ocean.

Our correlation analysis showed that small-particle backscatter is strongly aligned with chlorophyll concentration, reinforcing its use as an optical proxy for phytoplankton and their byproducts. In contrast, large-particle backscatter was only weakly correlated with chlorophyll, suggesting that its variability is driven by other processes such as aggregation, grazing, or physical transport. These findings highlight the importance of resolving particle size when interpreting backscatter data since total backscatter alone can mask key differences in export dynamics of high chlorophyll regions.

The detection of a subsurface chlorophyll maximum (SCM) provided further insight into the processes controlling productivity in the upper ocean. By comparing the depths of maximum backscatter and chlorophyll, we inferred the driver of the SCM without relying on nutrient or density profiles. This approach emphasizes the potential of particle-based measurements to uncover biological processes and stratification dynamics, even in the absence of traditional data. It also highlights the value of pairing particle distribution with chlorophyll measurements to better understand the processes controlling primary productivity.

In addition to biological insights, this method proved useful in detecting sediment resuspension features such as nepheloid layers. which are important for understanding the redistribution of particles and the physical processes that shape benthic environments. This also has implications for carbon burial, as sediment dynamics influence the stability and fate of organic material on the seafloor.

Our analysis of an unexpected, sustained productivity feature emphasizes the importance of considering large-scale physical drivers, such as ocean circulation, when studying regional productivity and carbon cycling. What initially appeared to be a small, localized zone of elevated productivity was ultimately linked to a basin-scale mechanism. The high concentration of large aggregates in this area suggests that it functions as an efficient carbon export zone. This highlights how even subtle changes in physical features, such as fronts or circulation boundaries, can create conditions that enhance particle aggregation and sinking. These findings reinforce the value of glider-based methods for detecting and investigating small-scale anomalies, which may largely influence regional carbon export.

Lastly, the comparison of two contrasting high-chlorophyll regions, one dominated by small particles, the other by large aggregates, illustrates the limitations of using chlorophyll alone to infer carbon export. Particle size, composition, and sinking behavior are critical for determining the fraction of organic carbon that reaches the deep ocean. Our method enables the isolation of these size-driven differences, helping identify regions with high carbon sequestration potential.

By providing a comprehensive view of particle dynamics in the upper ocean, this research links biological, geological, physical, and chemical processes to the broader question of how the ocean regulates the global carbon cycle. As climate change continues to influence atmospheric CO2 concentrations, understanding the ocean’s role in carbon sequestration will be critical for predicting the future trajectory of Earth’s climate system. This method represents an important step forward in oceanographic research, offering a more nuanced understanding of how particulate matter, nutrient cycling, and carbon export interact to influence the ocean's capacity to mitigate climate change.

6.3 Future work

Future studies should apply this method to additional glider missions within the C-PROOF program, particularly those operating in the same region and using identical optical sensors and platforms. These missions provide a ready-made opportunity to test the algorithm's robustness under varying seasonal conditions. For instance, several C-PROOF gliders have already collected the necessary optical backscatter and chlorophyll data along Line P and within the BC coastal region (Figure 6.1). Applying this algorithm to those missions would enable direct comparisons across time and space, offering insights into interannual variability in particle dynamics, aggregation, and carbon export potential.

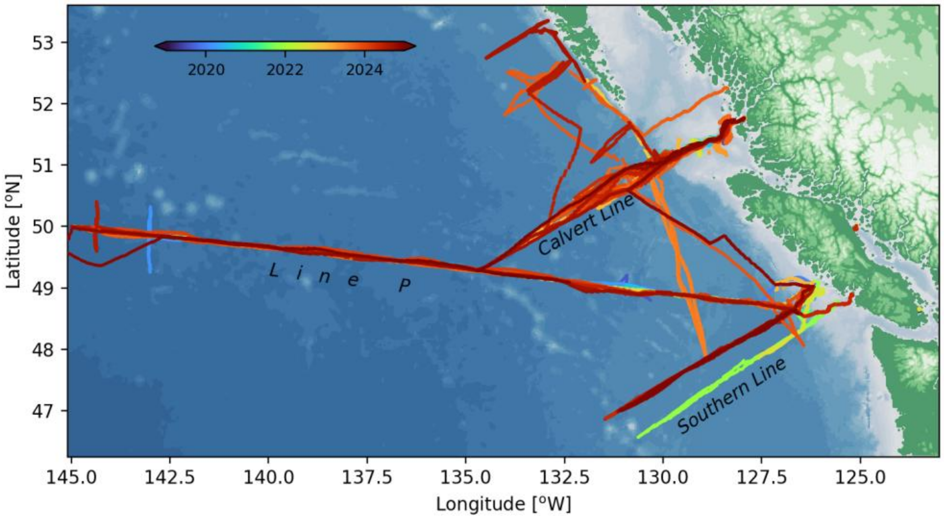

Figure 6.1 C-PROOF glider tracks (excluding an Arctic mission). Operating on three main lines, "Line P", "Calvert Line" and "Southern Line". Lines are colored by date, with red being more recent. (https://cproof.uvic.ca/observatory/)

Incorporating this method into the standard C-PROOF processing pipeline would be a significant step forward. By embedding the algorithm into the production of gridded datasets, it could generate size-resolved backscatter maps and identify large-aggregate hotspots in near real-time. This would enhance the scientific utility of the existing datasets and expand the capability of gliders to serve as autonomous platforms for carbon export monitoring. Further refinement of the method, particularly with respect to the filter size of the running minimum and maximum filters should be conducted to ensure that we are not inaccurately attributing high concentrations of small particles as larger aggregates. Investigation into refining the instrument noise should be conducted by collecting data from more deep casts where particle matter is extremely limited.

Regionally, this algorithm could be used to investigate particle dynamics in recurring features such as chlorophyll-rich frontal zones, subsurface chlorophyll maximums and areas of sediment resuspension on the shelf. It also provides a pathway to systematically flag and study anomalous productivity events. Targeted analyses of such features using long-term glider deployments would improve our understanding of episodic export events and their contribution to regional carbon cycling.

Long-term monitoring using this method could also be expanded to explore seasonal and interannual changes in particle size distributions, phytoplankton dynamics, and export efficiency across the northeast Pacific. This is particularly relevant in the context of climate-driven variability in stratification, nutrient delivery, and circulation patterns. Ultimately, by tracking where and when particles are transported deeper into the water column, this method can contribute to improved estimates of carbon sequestration and help quantify the role of the upper ocean in regulating atmospheric CO_2.

7. Acknowledgements

I would like to thank Dr. Roberta Hamme for her guidance and mentorship throughout this research. Her support and knowledge were instrumental to the development of this project. I am also deeply grateful to the Canadian-Pacific Robotic Ocean Observing Facility (C-PROOF) team, whose glider missions made this work possible. Their expertise and consultation were essential at multiple stages of the project. Finally, Thank you to the members of the Hamme Lab for their feedback, encouragement, and thoughtful discussions throughout the research process.

This research was funded by the Jamie Cassels Undergraduate Research Award (JCURA), which provided the opportunity and resources to pursue this work.

8. References

Anderson, G. C. (1969). SUBSURFACE CHLOROPHYLL MAXIMUM IN THE NORTHEAST PACIFIC OCEAN1. *Limnology and Oceanography*, *14*(3), 386–391. https://doi.org/10.4319/lo.1969.14.3.0386

Antoine, D., André, J.-M., & Morel, A. (1996). Oceanic primary production: 2. Estimation at global scale from satellite (Coastal Zone Color Scanner) chlorophyll. *Global Biogeochemical Cycles*, *10*(1), 57–69. https://doi.org/10.1029/95gb02832

Arjona-Camas, et al. (2022). Influence of Natural Processes and Bottom Trawling in the Nepheloid Layer Structure Off Vancouver Island (British Columbia, Canada, NE Pacific). *Frontiers in Marine Science*, *8*(770280). https://doi.org/10.3389/fmars.2021.770280

Ayers, J. M., & Lozier, M. S. (2010). Physical controls on the seasonal migration of the North Pacific transition zone chlorophyll front. *Journal of Geophysical Research*, *115*(C5). https://doi.org/10.1029/2009jc005596

Bach, L. T., et al. (2016). Influence of plankton community structure on the sinking velocity of marine aggregates. *Global Biogeochemical Cycles*, *30*(8), 1145–1165. https://doi.org/10.1002/2016gb005372

Barkmann, W., Schäfer-Neth, C., & Balzer, W. (2010). Modelling aggregate formation and sedimentation of organic and mineral particles. *Journal of Marine Systems*, *82*(3), 81–95. https://doi.org/10.1016/j.jmarsys.2010.02.009

Belkin, I. M., Cornillon, P. C., & Sherman, K. (2009). Fronts in Large Marine Ecosystems. *Progress in Oceanography*, *81*(1-4), 223–236. https://doi.org/10.1016/j.pocean.2009.04.015

Boyd, P. W., et al. (2019). Multi-faceted particle pumps drive carbon sequestration in the ocean. *Nature*, *568*(7752), 327–335. https://doi.org/10.1038/s41586-019-1098-2

Brewin, R. J. W., et al. (2012). Particle backscattering as a function of chlorophyll and phytoplankton size structure in the open-ocean. *Optics Express*, *20*(16), 17632. https://doi.org/10.1364/oe.20.017632

Briggs, N., Dall’Olmo, G., & Claustre, H. (2020). Major role of particle fragmentation in regulating biological sequestration of CO2 by the oceans. *Science*, *367*(6479), 791–793. https://doi.org/10.1126/science.aay1790

Briggs, N., et al. (2011). High-resolution observations of aggregate flux during a sub-polar North Atlantic spring bloom. *Deep Sea Research Part I: Oceanographic Research Papers*, *58*(10), 1031–1039. https://doi.org/10.1016/j.dsr.2011.07.007

Buesseler, K., et al. (1998). Upper ocean export of particulate organic carbon in the Arabian Sea derived from thorium-234. *Deep Sea Research Part II: Topical Studies in Oceanography*, *45*(10-11), 2461–2487. https://doi.org/10.1016/s0967-0645(98)80022-2

Canada,. (2017). *Line P Program*. Dfo-Mpo.gc.ca. https://www.dfo-mpo.gc.ca/science/data-donnees/line-p/index-eng.html

Claustre, H., et al. (2021). The Oceans’ Biological Carbon Pumps: Framework for a Research Observational Community Approach. *Frontiers in Marine Science*, *8*(780052). https://doi.org/10.3389/fmars.2021.780052

Clements, D. J., et al. (2022). Constraining the Particle Size Distribution of Large Marine Particles in the Global Ocean With *In Situ* Optical Observations and Supervised Learning. *Global Biogeochemical Cycles*, *36*(5). https://doi.org/10.1029/2021gb007276

Crawford, W. R., Brickley, P. J., & Thomas, A. C. (2007). Mesoscale eddies dominate surface phytoplankton in northern Gulf of Alaska. *Progress in Oceanography*, *75*(2), 287–303. https://doi.org/10.1016/j.pocean.2007.08.016

Crawford, W. R., Brickley, P., Peterson, T. D., & Thomas, A. P. (2005). Impact of Haida Eddies on chlorophyll distribution in the Eastern Gulf of Alaska. *Deep-Sea Research Part Ii-Topical Studies in Oceanography*, *52*(7-8), 975–989. https://doi.org/10.1016/j.dsr2.2005.02.011

D'Asaro, E., et al. (2011). Enhanced Turbulence and Energy Dissipation at Ocean Fronts. *Science*, *332*(6027), 318–322. https://doi.org/10.1126/science.1201515

dfo-rosie713. (2023). Uvic.ca. https://cproof.uvic.ca/gliderdata/deployments/dfo-rosie713/dfo-rosie713-20230810/

Diaz, B. P., et al. (2021). Seasonal mixed layer depth shapes phytoplankton physiology, viral production, and accumulation in the North Atlantic. *Nature Communications*, *12*(1). https://doi.org/10.1038/s41467-021-26836-1

Downing, J. (2006). Twenty-five years with OBS sensors: The good, the bad, and the ugly. *Continental Shelf Research*, *26*(17-18), 2299–2318. https://doi.org/10.1016/j.csr.2006.07.018

Durrieu de Madron, X., et al. (2017). Deep sediment resuspension and thick nepheloid layer generation by open-ocean convection. *Journal of Geophysical Research: Oceans*, *122*(3), 2291–2318. https://doi.org/10.1002/2016jc012062

Fischer, G., & Karakaş, G. (2009). Sinking rates and ballast composition of particles in the Atlantic Ocean: implications for the organic carbon fluxes to the deep ocean. *Biogeosciences*, *6*(1), 85–102. https://doi.org/10.5194/bg-6-85-2009

Fischer, G., et al. (2016). Deep ocean mass fluxes in the coastal upwelling off Mauritania from 1988 to 2012: variability on seasonal to decadal timescales. *Biogeosciences*, *13*(10), 3071–3090. https://doi.org/10.5194/bg-13-3071-2016

Freda, W. (2012). Spectral dependence of the correlation between the backscattering coefficient and the volume scattering function measured in the southern Baltic Sea. *Oceanologia*, *54*(3), 355–367. https://doi.org/10.5697/oc.54-3.355

Friedlingstein, P., et al. (2025). Global Carbon Budget 2024. *Earth System Science Data*, *17*(3), 965–1039. https://doi.org/10.5194/essd-17-965-2025

Giering, S. L. C., et al. (2020). Sinking Organic Particles in the Ocean—Flux Estimates From in situ Optical Devices. *Frontiers in Marine Science*, *6*. https://doi.org/10.3389/fmars.2019.00834

Karakaş, G. et al. (2009). Impact of particle aggregation on vertical fluxes of organic matter. *Progress in Oceanography*, *83*(1-4), 331–341. https://doi.org/10.1016/j.pocean.2009.07.047

Hayashi, Y., et al. (2023). Cohesive bond strength of marine aggregates and its role in fragmentation. *Frontiers in Marine Science*, *10*. https://doi.org/10.3389/fmars.2023.1167169

Henson, S., et al. (2024). Knowledge Gaps in Quantifying the Climate Change Response of Biological Storage of Carbon in the Ocean. *Earth S Future*, *12*(6). https://doi.org/10.1029/2023ef004375

How do floats work. (n.d.). Argo. https://argo.ucsd.edu/how-do-floats-work/

Huang, B., et al. (2020). NOAA 0.25-degree Daily Optimum Interpolation Sea Surface Temperature (OISST), Version 2.1. SST. NOAA National Centers for Environmental Information. https://doi.org/10.25921/RE9P-PT57

Howard, E., Emerson, S., Bushinsky, S., & Stump, C. (2010). The role of net community production in air-sea carbon fluxes at the North Pacific subarctic-subtropical boundary region. *Limnology and Oceanography*, *55*(6), 2585–2596. https://doi.org/10.4319/lo.2010.55.6.2585

Kwon, E. Y., Primeau, F., & Sarmiento, J. L. (2009). The impact of remineralization depth on the air–sea carbon balance. *Nature Geoscience*, *2*(9), 630–635. https://doi.org/10.1038/ngeo612

Liu, Y., Zheng, Q., & Li, X. (2021). Characteristics of Global Ocean Abnormal Mesoscale Eddies Derived From the Fusion of Sea Surface Height and Temperature Data by Deep Learning. *Geophysical Research Letters*, *48*(17). https://doi.org/10.1029/2021gl094772

Mantovanelli, A., & Thomson, P. (2016). *Particle backscattering coefficient For Wetlab Ecopucks in IMOS ANFOG gliders*. https://doi.org/10.13140/RG.2.1.4875.5440

Martin, J. H., et al. (1987). VERTEX: carbon cycling in the northeast Pacific. *Deep Sea Research Part A. Oceanographic Research Papers*, *34*(2), 267–285. https://doi.org/10.1016/0198-0149(87)90086-0

Martin, J., et al. (2010). Prevalence, structure and properties of subsurface chlorophyll maxima in Canadian Arctic waters. *Marine Ecology Progress Series*, *412*, 69–84. https://doi.org/10.3354/meps08666

Masuda, Y., et al. (2021). Photoacclimation by phytoplankton determines the distribution of global subsurface chlorophyll maxima in the ocean. *Communications Earth & Environment*, *2*(1), 1–8. https://doi.org/10.1038/s43247-021-00201-y

Nowicki, M., DeVries, T., & Siegel, D. A. (2022). Quantifying the carbon export and sequestration pathways of the ocean's biological carbon pump. *Global Biogeochemical Cycles*, *36*(3). https://doi.org/10.1029/2021gb007083

Oschlies, A., & Garçon, V. (1998). Eddy-induced enhancement of primary production in a model of the North Atlantic Ocean. *Nature*, *394*(6690), 266–269. https://doi.org/10.1038/28373

Perry, M. J., et al. (2008). Seaglider observations of blooms and subsurface chlorophyll maxima off the Washington coast. *Limnology and Oceanography*, *53*(5part2), 2169–2179. https://doi.org/10.4319/lo.2008.53.5_part_2.2169

Platforms. (2025). Uvic.ca. https://cproof.uvic.ca/platforms/

Polovina, J. J., et al. (2001). The transition zone chlorophyll front, a dynamic global feature defining migration and forage habitat for marine resources. *Progress in Oceanography*, *49*(1-4), 469–483. https://doi.org/10.1016/s0079-6611(01)00036-2

Puig, P., et al. (2004). Role of internal waves in the generation of nepheloid layers on the northwestern Alboran slope: Implications for continental margin shaping. Journal of Geophysical Research: Oceans, 109(C9). https://doi.org/10.1029/2004JC002394

Richardson, K., & Bendtsen, J. (2019). Vertical distribution of phytoplankton and primary production in relation to nutricline depth in the open ocean. *Marine Ecology Progress Series*, *620*, 33–46. https://doi.org/10.3354/meps12960

Ross, T., Craig, S. E., Comeau, A., Davis, R., Dever, M., & Beck, M. (2017). Blooms and subsurface phytoplankton layers on the Scotian Shelf: Insights from profiling gliders. *Journal of Marine Systems*, *172*, 118–127. https://doi.org/10.1016/j.jmarsys.2017.03.007

Sackmann, B. S., Perry, M. J., & Eriksen, C. C. (2008). Seaglider observations of variability in daytime fluorescence quenching of chlorophyll-*a* in Northeastern Pacific coastal waters. *Biogeosciences Discuss*, *5*, 2839–2865. https://doi.org/10.5194/bgd-5-2839-2008

Sarah, & Humphreys, M. (2017). Biological Pump. *Encyclopedia of Earth Sciences*, 1–6. https://doi.org/10.1007/978-3-319-39193-9_154-1

Scattering Meter BB9 User's Guide. (n.d.). https://www.comm-tec.com/prods/mfgs/Wetlabs/Manuals/Eco-BB9_manual.pdf

Schober, P., Boer, C., & Schwarte, L. A. (2018). Correlation coefficients: Appropriate Use and Interpretation. *Anesthesia & Analgesia*, *126*(5), 1763–1768. https://doi.org/10.1213/ANE.0000000000002864

Shiv Priyam Raghuraman, Soden, B., Clement, A., Vecchi, G., Menemenlis, S., & Yang, W. (2024). The 2023 global warming spike was driven by the El Niño–Southern Oscillation. *Atmospheric Chemistry and Physics*, *24*(19), 11275–11283. https://doi.org/10.5194/acp-24-11275-2024

Siegel, D. S., et al. (2022). Quantifying the Ocean's Biological Pump and Its Carbon Cycle Impacts on Global Scales. *Annual Review of Marine Science*, *15*(1), 329–356. https://doi.org/10.1146/annurev-marine-040722-115226

Slocum G2 Glider Operators Manual. (2012). http://gliderfs.coas.oregonstate.edu/gliderweb/docs/slocum_manuals/Slocum_G2_Glider_Operators_Manual.pdf

St. Laurent, L., & Merrifield, S. (2017). Measurements of Near-Surface Turbulence and Mixing from Autonomous Ocean Gliders. *Oceanography*, *30*(2), 116–125. https://doi.org/10.5670/oceanog.2017.231

Takeuchi, M., et al. (2019). Turbulence mediates marine aggregate formation and destruction in the upper ocean. *Scientific Reports*, *9*(1). https://doi.org/10.1038/s41598-019-52470-5

Thomalla, S. J., Moutier, W., Ryan-Keogh, T. J., Gregor, L., & Schütt, J. (2017). An optimized method for correcting fluorescence quenching using optical backscattering on autonomous platforms. *Limnology and Oceanography: Methods*, *16*(2), 132–144. https://doi.org/10.1002/lom3.10234

Venkat Shesu, R., et al. (2021). An improved method for quality control of in situ data from Argo floats using α convex hulls. *MethodsX*, *8*, 101337–101337. https://doi.org/10.1016/j.mex.2021.101337

Viljoen, J. J., Sun, X., & Robert. (2024). Climate variability shifts the vertical structure of phytoplankton in the Sargasso Sea. *Nature Climate Change*, *14*. https://doi.org/10.1038/s41558-024-02136-6

Wang, Y., et al. (2019). Phytoplankton Blooms off a High Turbidity Estuary: A Case Study in the Changjiang River Estuary. *Journal of Geophysical Research: Oceans*, *124*(11), 8036–8059. https://doi.org/10.1029/2019jc015343

Weber, T., et al. (2016). Deep ocean nutrients imply large latitudinal variation in particle transfer efficiency. *Proceedings of the National Academy of Sciences*, *113*(31), 8606–8611. https://doi.org/10.1073/pnas.1604414113

Ye, R., Zhou, F., Ma, X., Liu, C., Meng, Q., Tian, D., Guo, R., Li, H., Shou, L., Du, P., & Lwin, S. M. (2024). Effect of Turbulent Mixing on the Formation of Intermediate Nepheloid Layer over the Northern Continental Slope of the Andaman Sea. *Deep Sea Research Part I Oceanographic Research Papers*, *212*, 104376. https://doi.org/10.1016/j.dsr.2024.104376

Zhang, H.-R., Wang, Y., Xiu, P., Qi, Y., & Chai, F. (2021). Roles of Iron Limitation in Phytoplankton Dynamics in the Western and Eastern Subarctic Pacific. *Frontiers in Marine Science*, *8*, 735826. https://doi.org/10.3389/fmars.2021.735826